Fall 2019

Study of optical propulsion concepts and techniques for small-satellites

Jaykob Neil Maser

Department: Mechanical and Aerospace Engineering

STUDY OF OPTICAL PROPULSION CONCEPTS AND TECHNIQUES FOR SMALL-SATELLITES

by

JAYKOB NEIL MASER

A DISSERTATION

Presented to the Faculty of the Graduate School of the

MISSOURI UNIVERSITY OF SCIENCE AND TECHNOLOGY

In Partial Fulfillment of the Requirements for the Degree

DOCTOR OF PHILOSOPHY

in

AEROSPACE ENGINEERING

2019

Approved by:

Joshua Rovey, Co-Advisor
Xiaodong Yang, Co-Advisor
Monica Allen
Jie Gao
Hank Pernicka

ABSTRACT

The first objective of this research is to manufacture and investigate the characteristics and use of asymmetric, metallic, nanostructures for plasmonic force propulsion, a developing method of nano-/picosatellite thrust generation. This project developed a higher-fidelity model of a recently envisioned small spacecraft propulsion system for precision pointing and proximity control. Plasmonic force propulsion harnesses solar light focused onto plasmon reactive sub-wavelength nanostructures to generate polarized oscillations of electrons on the surface of metallic nanostructures which accelerate and expel nanoparticle propellant via strong optical forces. This research also explores how material selection affects the electromagnetic response of the closely positioned asymmetric nanostructures.

Furthermore, a dielectrophoretic (DEP) nanoparticle injector concept and its use in a plasmonic/photonic-based nanoparticle manipulation system is also described. Particle motion is achieved by generating an electrostatic, non-uniform field between two tilted plates and applying the corresponding DEP force to net-neutral nanoparticles. We investigate the dependence the DEP force has on the plate angle of the charged plates as well as their separation distance, dielectric filler material, and exit interface membrane.

Finally we investigate a plasmonic particle acceleration scheme aimed at manipulating high-mass, charged particles such as ions. Analogous to the Alvarez linear accelerator, this plasmon LINAC attempts to harness traveling waves confined to the interior surface of a cylindrical hole in a metallic thin film to impart energy to a low energy, massive particle.

ACKNOWLEDGMENTS

I offer my sincere thanks to my research co-advisor, Dr. Rovey, for his encouragement and mentorship throughout my graduate career. I would like to thank Dr. Jeffery Allen, Dr. Monica Allen, and Dr. Simeon Trefandilov for their guidance, feedback, time, and use of computational resources. I am also thankful to my co-advisor Dr. Xiaodong Yang and the rest of my advising committee: Dr. Jie Gao, and Dr. Hank Pernicka for their support and guidance. I would like to acknowledge the financial support of the Air Force Office of Scientific Research for partially supporting this work through grant FA9550-14-1-0230 with Dr. Mitat Birkan as program monitor and the NASA Innovative Advanced Concepts program for partially supporting this work through grant NNX16AL26G. Additionally, I would like to thank the Missouri University of Science and Technology for sponsoring my graduate program through the Chancellor's Fellowship.

I would also like to thank my fellow peers: Alex Mundahl, Mitch Wainwright, and Zach Gill for their friendship, support, and willingness to entertain half-baked research ideas. My parents and in-laws who have encouraged me in the times I struggled to continue and reveled with me when I succeeded. I am grateful to my wife, Shannah, for being an integral part of my life and for motivating me throughout my graduate experience. Above all I want to offer this endeavor to God for the wisdom, strength, and perseverance he blessed me with.

TABLE OF CONTENTS

Page

LIST OF ILLUSTRATIONS

Page

LIST OF TABLES

Page

NOMENCLATURE

Symbol	Description
A	Absorptance
A_n	Constants
A_{nano}	Area of the Nano-unit
$\vec{a}_{nano}$	Acceleration due to the Nano-unit
B	Magnetic Induction Field
B_θ	Azimuthal Magnetic Field
b	Plate Length
CORp	Coefficient of Restitution of the Particle
CORw	Coefficient of Restitution of the Wall
c	Speed of Light
d	Capacitor Plate Separation
$d\omega/dk$	Group Velocity
E	Electric Field
E_{cap}	Electric Field in a Parallel Plate Capacitor
E_r	Radial Electric Field
E_z	Longitudinal Electric Field
e	Electron Charge
$\vec{F}_{DEP}$	Dielectrophoretic Force
F_y	Force in y-direction
F_z	Force in z-direction

f_{pars}	Force Acting on a Particle during Particle-Particle Collision
f_{wall}	Force Acting on a Particle during Particle-Wall Collision
g	Gap Size between Nanostructures / Gravitational Acceleration
$H_1^{(1)}$	Bessel Function of the Second Kind
I_{leo}	Solar Radiation Intensity in Low Earth Orbit
i, j	Imaginary Number
J_n	Bessel Function of the First Kind
k	Clausius-Mossotti Factor
$\vec{k}$	Wave Number
k_{ns}	Nanostructure Thermal Conductivity
k_p	Wave Number Corresponding to Plasma Frequency
k_{sp}	Surface Plasmon Wave Number
k_{sub}	Substrate Thermal Conductivity
l	Length of Nanostructures
m	Diffraction Mode Number / Mass
m^*	Effective Electron Mass
Np	Number of Particles
n	Charge Carrier Density / Index of Refraction
P_{nano}	Solar Power Imparted to Nano-unit
Q	Charge on the Plate
R	Reflectance / Radius of Nanoparticle
$\vec{r}$	Position Vector

$\vec{r}_L{}'$	Lower Plate Position Vector
$\vec{r}_U{}'$	Upper Plate Position Vector
s_{ns}	Nanostructure Thickness
s_{sub}	Substrate Thickness
T	Transmittance / Temperature
T_e	Environment Temperature
t_{sh}	Shutter Speed
u	Pre-collision Velocity
V	Electric Potential Difference
v	Velocity
v_{f_1}	Final Velocity of Particle after First Nano-unit
v_p	Particle Velocity
w	Width of Nanostructures
γ	Damping Factor
Δx_a	Acceleration Path Length
δ_{ij}	Kronecker Delta
ε	Emissivity of the Material
ε_∞	High Frequency Dielectric Permittivity
ε_0	Permittivity of Free Space
ε_r	Relative Dielectric Permittivity
ε_{st}	Static Permittivity
θ	Incident Angle

λ_L	Laser Wavelength
ν	Relaxation Time
σ	Stefan-Boltzmann Constant
φ	Polar Angle
ω	Angular Frequency of Traveling Wave
ω_0	Resonant Frequency
ω_p	Plasma Frequency
ω_{sp}	Surface Plasmon Frequency
∇	Del Operator
∇_ϵ	Amplitude Factor / Oscillator Strength

1. INTRODUCTION

Nanosatellites are defined as spacecraft with a mass of 1-10 kg. The demand for and use of these and other small satellites is widespread and is projected to continue increasing according to numerous SpaceWorks reports on the nano/microsatellite market.[1,2,3] The 2018 SpaceWorks report[2] also makes note that most nano/microsatellites are launched in large clusters and that large constellations of small satellites for communications and/or observations purposes will make up ~70 % of the market over the next five years. Satellites within sizeable constellations will need the ability to maneuver and orient themselves precisely in relation to the other satellites of the cluster. In spite of the intense and exploding interest in small spacecraft, their full potential remains untapped because they lack maneuverability. The major challenge remains propulsion. Micci and Ketsdever[4] compiled micropropulsion state-of-the-art in 2000 and many of those micropropulsion systems have been or are being investigated for small spacecraft (e.g., microresistojets, microcavity discharge thrusters, mini ion/Hall, pulsed plasma thrusters, and electrospray MEMS). New concepts have also been investigated (e.g., nanoparticle field extraction, laser ablation, free molecule resistojet). While significant advances have been made, small spacecraft still lack propulsion for the same reasons outlined by Micci and Ketsdever: mass, power, and volume constraints. The need remains for a propulsion system that can fit on ever-shrinking small satellite platforms. We investigate the feasibility of a plasmonic force propulsion system to fit this niche.

Plasmonic manipulation and acceleration of particles stands on the growing field of plasmonics, which exploits the unique interactions of light with metallic

nanostructures. When focused optical radiation strikes the surface of a metal, the oscillating electric field component of the radiation will cause the surface electrons in the metal to oscillate. A quantized oscillation of a group of these electrons is called a plasmon, like a photon is a quantized unit of electromagnetic oscillation. The interaction between a substance and an incident electromagnetic wave, composed of orthogonal electric and magnetic field components (Figure 1.1a), is determined by the complex relative permittivity of the material.

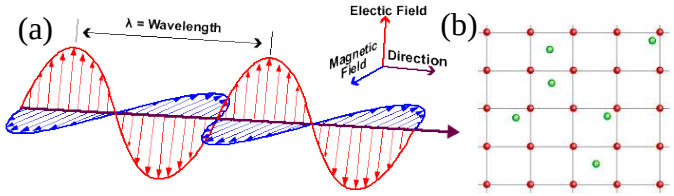

Figure 1.1: Light-matter interaction physics (a) electromagnetic wave components and (b) free electron material.

The permittivity defines how the strength and propagation of the incident electric field is affected by the substance, relative to free space. A well accepted model for the

$$\varepsilon(\vec{k},\omega) = 1 - \frac{{\omega_p}^2}{\omega^2 + i\nu\omega} \tag{1}$$

complex relative permittivity of a material with free electrons, like a gaseous or solid-state plasma, is the Drude model with the dielectric constant, or relative permittivity, given in Eqn. (1), where ω_p is the plasma frequency. In the presence of an external electric field, the electrons in a metal are displaced from their equilibrium positions and

when they are pulled back by the restoring force exerted on them by the nuclei they will overshoot due to their inertia and will oscillate with a characteristic frequency, the plasma frequency. ω is the angular frequency of the traveling wave in the material. i is the imaginary number $\sqrt{-1}$. ν is the relaxation time of the electrons. $\vec{k}$ is the wave number (inverse of wavelength) of the propagating wave. The Drude model treats the electrons in a metal as identical, distinguishable, free particles moving in a constant potential background of fixed nuclei (Figure 1.1b) and applies classical Maxwell-Boltzmann statistics to them. For incident electromagnetic radiation with angular frequency much higher than the plasma frequency, material losses vanish and the metal appears to be transparent, or weakly absorbing. This is indicative of a free electron gas. For angular frequencies lower than the plasma frequency, metals behave like good conductors and shield, or block out, the electromagnetic radiation. When damping is negligible, the relaxation time goes to zero and the Drude model dielectric constant reduces to Eqn. (2).

$$\varepsilon\left(\vec{k}, \omega\right) = 1 - \frac{{\omega_p}^2}{\omega^2} \tag{2}$$

Plasmons can also exist along the surface of a metal at its interface with a dielectric. This is known as a surface plasmon polariton. A surface plasmon is a non-propagating collective electron oscillation near or at the surface of a metal and a polariton is a coupled state between an elementary excitation and a photon also known as a light-matter interaction. Plasmons are excited by the oscillating electric field of incident electromagnetic radiation that must have nonzero y- and z-components of the electric

field which is known as transverse magnetic or p-polarized. The SPP's propagate along the interface and exponentially decay into the metal and dielectric regions perpendicular to the interface. The oscillating electron density generates a localized electromagnetic field near the interface that can be utilized to accelerate nanoparticles. The electromagnetic field can be tuned by changing the size and shape of the nanostructures and used to control the motion of particles within the vicinity of the nanostructure.

1.1. TRADITIONAL PARTICLE ACCELERATORS

The following section begins with a short review of traditional particle accelerators and then focuses on novel, tabletop accelerators; specifically optical accelerating mechanisms.

The most basic particle acceleration mode is that of electrostatic acceleration. This acceleration mechanism uses a stationary electric field, such as the field corresponding to the electric potential between two infinitely large plates where one is positively charged and the other is grounded (or negatively charged) such as the plates shown in Figure 1.2. The case of infinitely extended plates is the ideal case whereas what is shown in Figure 1.2 can, more or less, be approximated as such if the acceleration length is much less than the width of the plates. The triangular bulge on the left plate indicates the particle source (electrons in this case) and there is a corresponding hole in the right plate so that the accelerated electron can pass through the plate for further use. The electron experiences acceleration due to the Coulomb force, generated by the electric potential difference between the two plates. The energy that is gained by the electron is simply the charge of the electron times the potential difference of the electric field.

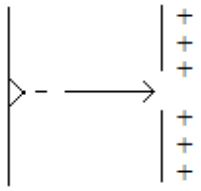

Figure 1.2: Example configuration of an electrostatic accelerator.

In contrast to the electrostatic accelerating scheme, dynamic acceleration utilizes a time dependent electromagnetic field to impart energy to the particle and provide control over its motion during acceleration.

1.1.1. Linear Accelerator (LINAC). The linear accelerator uses an oscillatory electromagnetic field to impart energy to a traveling particle. An oscillatory field exhibits both accelerating and decelerating phases. Therefore, in order to avoid the decelerating phase, many LINACs make use of metallic drift tubes that shield the traveling particle from the oscillatory field during the deceleration phase (Figure 1.3). The drift length between the accelerating gaps increases as the particle velocities become greater, up to the point in which relativistic considerations become significant.

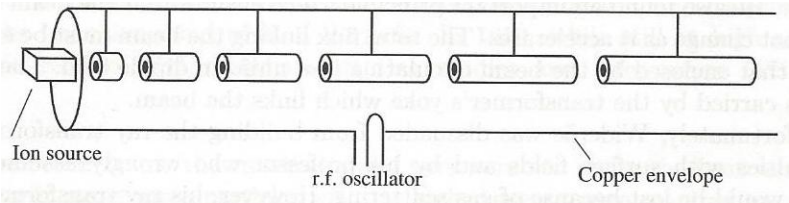

Figure 1.3: Schematic of an Alvarez LINAC concept.

1.1.2. Synchrotron. The synchrotron, Figure 1.4,[5] is a dynamic particle accelerator that makes use of three distinct dynamic mechanisms: 1) accelerating gaps

between drift tubes, 2) variable frequency electric field, and 3) variable strength magnetic field [5,6]. Like the LINAC, there are accelerating and decelerating phases because the electric field used in the dynamic acceleration scheme is time dependent. Drift tubes

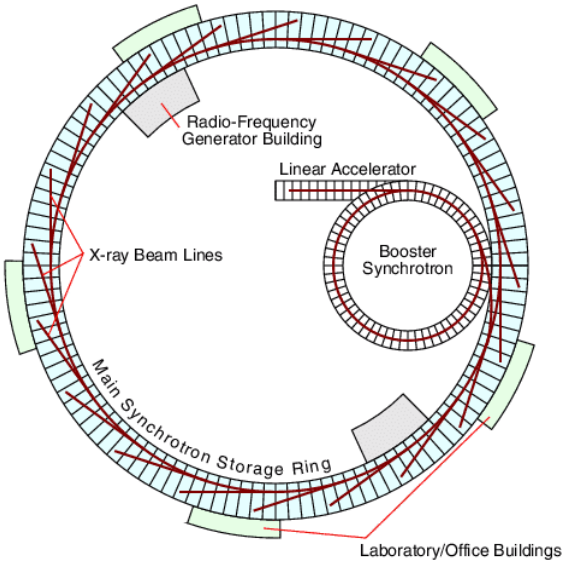

Figure 1.4: Top down view of a synchrotron accelerator facility.

allow the particle to gain energy from the acceleration phase while shielding the particle from deceleration during the interaction. These drift tubes are located around the ring of the synchrotron. A variable frequency electric field is used so that the field remains matched to the particle phase as the particles accelerate around the ring. Using a variable strength magnetic field allows the accelerating particles to be held in a constant radius.

1.2. OPTICAL PARTICLE ACCELERATORS

In this section, a variety of tabletop accelerator concepts will be shared from the literature. The larger electric field gradients that are achievable with

laser/plasma/dielectric systems are highly desirable because smaller accelerating infrastructures can be developed without decreasing the maximum achievable particle energy. These concepts consist of: dielectric accelerating structures geometrically arranged so that they exhibit a photonic bandgap; plasmonic accelerators that make use of metallic metasurfaces to alter the produced electric field; photonic gratings that utilize Bragg reflections; the plasmon LINAC and plasmonic force propulsion device that utilize a solid-state plasma; and target normal sheath acceleration for heavy-ion acceleration.

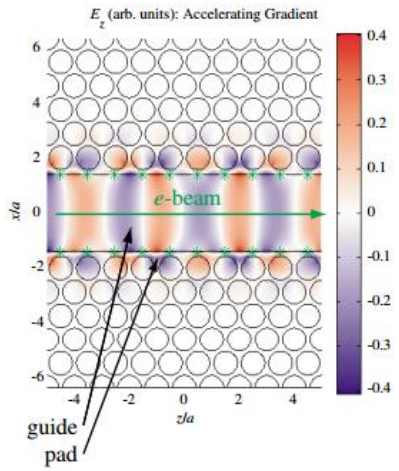

Figure 1.5: The electric field produced in a 2D photonic crystal accelerator.

1.2.1. 2-D Photonic Crystal Accelerators. In Cowan's article [7], a specific class of photonic crystal accelerating structures called two-dimensional structures is explored. The 2-D photonic crystal accelerator is composed of dielectric materials which are more resilient than metals to electric breakdown under the influence of the large electric fields produced by laser radiation. The structure that Cowan studies, Figure 1.5, is composed of an infinite lattice of holes in a dielectric, with a vacuum waveguide cut into the lattice

through which the laser beam propagates and by which the photonic crystal produces a speed-of-light mode that couples to a relativistic electron beam. Electromagnetic modes that are allowed to propagate through the dielectric lattice fall into discrete bands, much like the electronic states in a solid. This implies that a band gap of non-propagating modes exist within the structure, as shown by Cowan [7].

1.2.2. Non-Resonant Focusing. Also, related to the propagation of accelerating modes in a photonic crystal structure, Naranjo, et. al. [8], studied the effects of a non-resonant mode that does not contribute to acceleration but does cause focusing of the

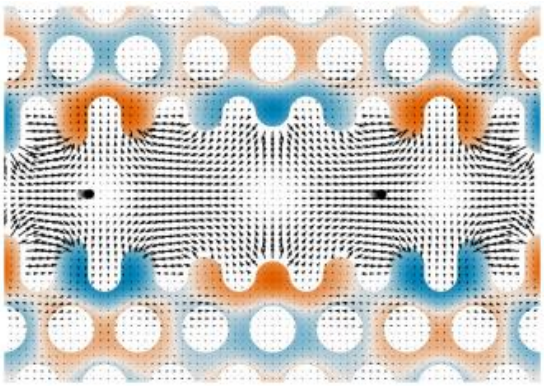

Figure 1.6: Electric field profile of a photonic crystal accelerator with harmonic acceleration and non-resonant focusing.

beam. They propose a geometric setup that supports multiple spatial harmonics (Figure 1.6) so that second-order focusing provided by non-resonant harmonics can be used to overcome the defocusing characteristics of the resonant harmonic. The particle shown in Figure 1.6 experiences an accelerating force to the right, as seen by the arrows representing the electric field. It also experiences a focusing effect toward the center of

the waveguide such that if the particle represented a bunch of particles, then the bunch would tend to hold together in the transverse direction and not be pulled apart.

1.2.3. Plasma Wake-Field Accelerator. Figure 1.7 illustrates a plasma wake-field acceleration concept. Pae, Choi, and Lee present simulations, in their paper [9], of a particle accelerator that transitions from a laser wake-field accelerator to a plasma wake-field accelerator. In this mechanism, a laser pulse is sent to propagate through a plasma medium. The pulse interacts with the plasma in such a way that it produces high-energy electrons that cause a plasma wake-field to arise. This plasma wake-field traps electrons and accelerates them as it travels behind the propagating laser pulse. The dotted circles in Figure 1.7 indicate trapped electron bunches that are accelerated with the propagating plasma wake-field.

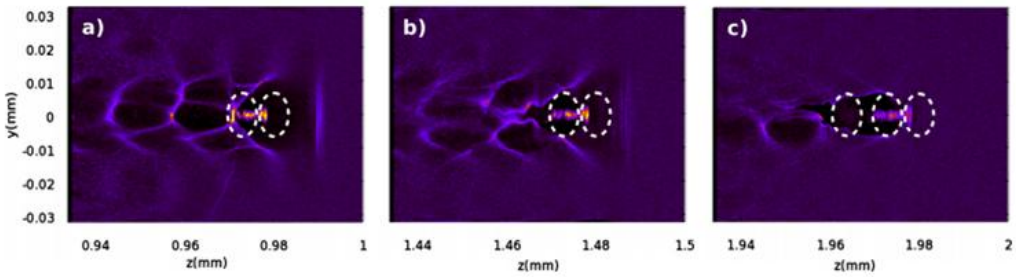

Figure 1.7: Snapshots of electron bunches traveling in a plasma wake-field accelerator.

1.2.4. Plasmonic Meta-Surface Accelerator. Bar-Lev and Scheuer [10] propose an accelerator scheme that is based on plasmonic nanoantennas. The laser-driven structure uses the focusing abilities of the nanoantennas to enhance the localized electric field and add energy to relativistic particles. The researchers utilize the plasmonic resonance of the structure to enhance the near-field zone and overcome losses due to the

metallic nanoantennas. They propose a metasurface of nanoantennas that enhance the local electric field about the region of the nanoantennas and directs the field towards the vacuum accelerating cavity. The structure is designed to accelerate relativistic electrons though the researchers claim that smaller geometrical unit cells could allow for the acceleration of slower particle beams [10]. The unit cell depicted in the cutout of Figure 1.8 is approximately the length, dy, of the center laser wavelength that is used so that a spatial harmonic is produced to couple with the speed-of-light propagation.

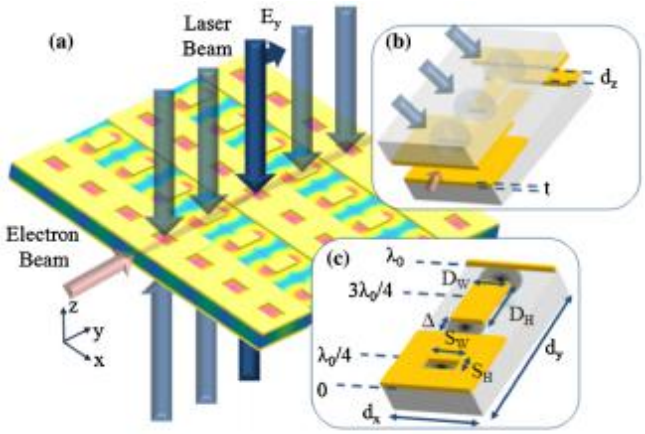

Figure 1.8: The unit cell geometry and distribution of a plasmonic metasurface accelerator.

1.2.5. Cylindrical Bragg Grating Accelerator. Mizrahi and Schächter describe an accelerating waveguide that is composed of a stack of dielectric layers [11]. They achieve confinement of the accelerating fields for optical wavelengths by use of the Bragg reflection phenomenon. This is the same effect observed in the x-ray diffraction experiments of crystals. The cylindrical Bragg accelerator, shown in Figure 1.9, contains a vacuum region, where the accelerated beam propagates, and concentric layers of loss-

less dielectric material surrounding the accelerating region. Large accelerating fields, confined to the center vacuum region, occur when the incident laser radiation is reflected off of the interfaces between the dielectric materials and constructively interfere.

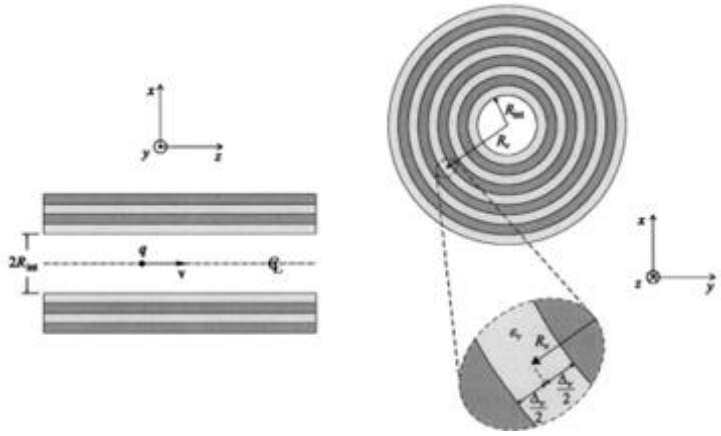

Figure 1.9: The layer profile of a cylindrical Bragg grating accelerator.

1.2.6. Target Normal Sheath Acceleration (TNSA). TNSA is a particle accelerating mechanism that is very simple in experimental setup but for which the physics of the interaction are still intensely studied. TNSA produces a well-behaved beam of ions, primarily protons, which is emitted and accelerated from the back surface of a thin film. A high intensity laser pulse strikes the front side of the metallic film where a plasma plume is created by the leading edge of the laser pulse. The primary signal of the laser pulse then interacts with the plasma plume and its energy is converted to kinetic energy in the form of hot electrons (~ a few MeV). These relativistic, collisionless electrons propagate back and forth in the film, creating a cloud at the surfaces of the film, which extends into the surrounding vacuum a few Debye lengths. The charge separation produced by the hot electrons outside the film and the positively charged ions left within

the film generates an intense electric field pointing normally away from the surface of the film. This intense electric field rips light ions, such as protons from surface contaminants, off the film and accelerates them away from the interaction area [12,13]. This predominantly occurs at the back side of the target film but some researchers have shown acceleration from the front side as well [12]. This accelerating mechanism is illustrated in Figure 1.10.

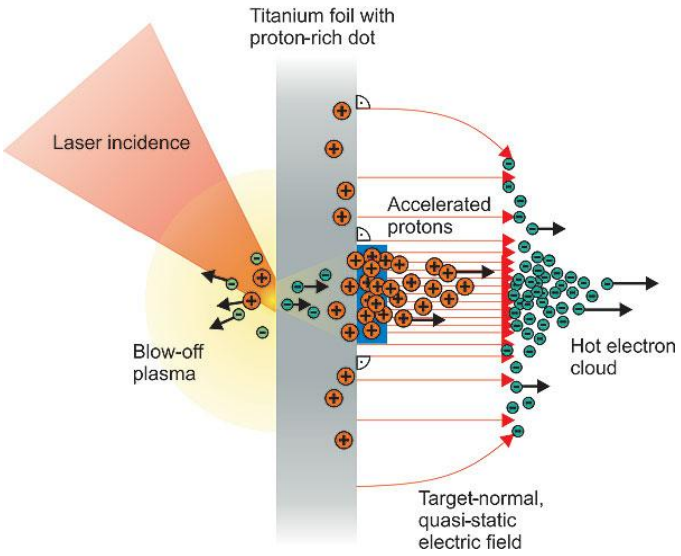

Figure 1.10: A schematic of the Target Normal Sheath Acceleration physics.

Similar to the plasmonic metasurface, the plasmonic force propulsion (PFP) device and the plasmon LINAC make use of electromagnetic oscillations confined to the interface between a metal and a dielectric that are excited by incident radiation. The PFP confines these oscillations, or surface plasmon polaritons (SPP's), to the upper surface of a trapezoidal nanostructure whereas the plasmon LINAC utilizes a cylindrical geometry.

1.2.7. Plasmonic Force Propulsion. In the PFP device, Figure 1.11, a lens is used to focus solar radiation onto subwavelength metallic nanostructures that are

fabricated to resonantly interact and couple with the incident light which excites SPP's on the surface of the metallic nanostructures. The SPP's create a non-uniform electro-

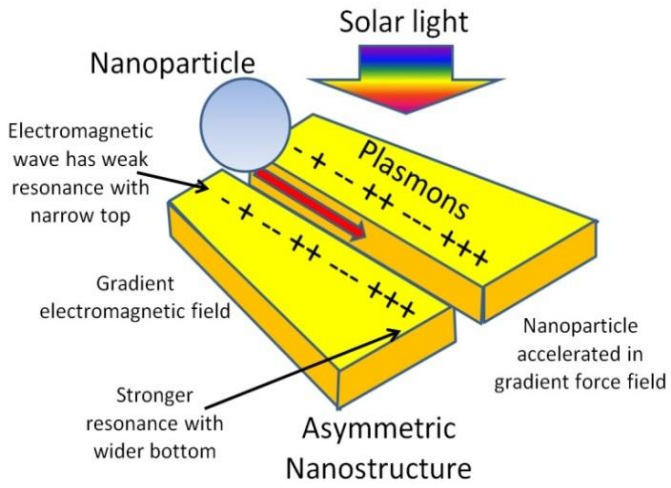

Figure 1.11: The plasmonic force propulsion concept.

magnetic force field that causes net-neutral nanoparticles to be accelerated and expelled from the region of the nanostructure.

1.2.8. Plasmon LINAC. For the plasmon LINAC, the particle beam is directed through a cylindrical hole, cut into a thin film (Figure 1.12), following a laser pulse that

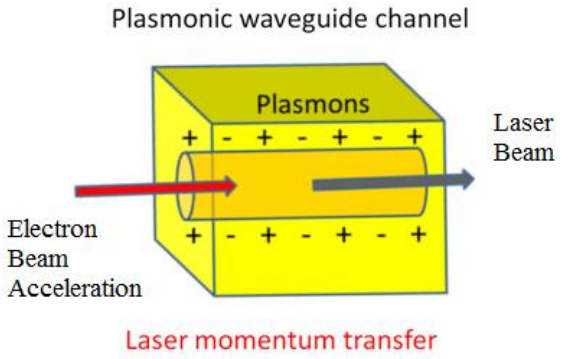

Figure 1.12: The geometry of the cylindrical plasmon LINAC geometry.

excites SPP's along the cylindrical surface, which also travel through the hole. The electron beam propagates with the SPP's and is accelerated along the length of the hole. Most of the SPP modes in this setup travel near the speed of light, therefore only particles with velocities above a certain cutoff can be coupled to and excited.

1.2.9. Low Speed Optical Acceleration. The plot in Figure 1.13 serves to compare a slew of accelerators from the above fields mentioned. The generated field gradient of each accelerator is plotted versus the physical size of the structure.

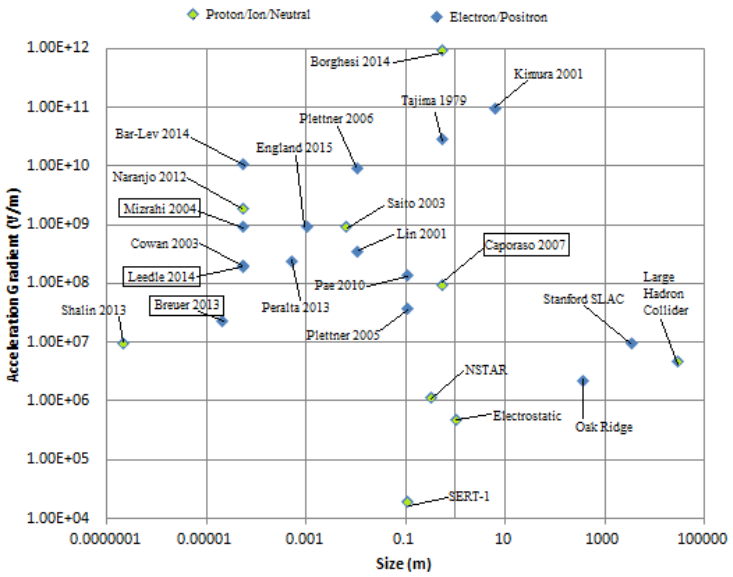

Figure 1.13: Acceleration gradient vs. structure size of particle accelerators.

The four boxed data points in Figure 1.13 indicate accelerators that are capable of velocity matching with nonrelativistic particles. Of these four accelerators, three are restricted to velocities above ~0.3c (8.99×10^7 m/s), and the fourth (Caporaso 2007) is a non-optical accelerator. If the goal for particle accelerating mechanisms is to produce a complete accelerating scheme on a table, then much progress is yet needed in the

research of synchronizing with slow particle velocities. The same staged acceleration that is used on electrons: conventional electrostatic acceleration, followed by RF, followed by optical means, needs to be developed for particles with appreciable mass.

2. NET-NEUTRAL PARTICLE ACCELERATION

2.1. NEUTRAL ACCELERATION BACKGROUND

Photonic systems are actively researched because of promising capabilities such as linking optoelectronic interactions for enhanced computing through plasmonics, and enabling lab-on-a-chip through manipulation of microparticles by gradient electromagnetic fields. Plasmonics is well-known in its ability to focus electromagnetic radiation beyond the diffraction limit[14] and to advance particle manipulation through the use of "plasmon nano-optical tweezers"[15] which utilizes localized surface plasmon resonances to create trapping volumes, or potential wells, and trap particles in the vicinity of symmetric nanostructures.[16] An asymmetric, V-groove type structure was developed by Shalin and Sukhov in 2012 [17] for the one dimensional acceleration and ejection of nanoparticles out of the V-grooves in a nanocannon fashion. They propose that ejection of nanoparticles from the V-grooves will occur due to the gradient force of the E-field in the grooves and a negative real part of the polarizability of the nanoparticles. In an early paper, they numerically calculated the maximum exit velocity of the particles ejected from these V-grooves to be approximately 11 cm/s in air[17] and further refined the estimate to be on the order of 1 m/s with optical excitation between 300 – 400 nm. [18] The focus of this dissertation is to investigate a nanoparticle manipulation scheme that makes use of asymmetric nanostructures to generate gradient plasmonic force fields for the acceleration of net-neutral nanoparticles via dielectrophoresis with applications in nanosatellite propulsion systems[19-21]. Unlike Shalin's V-groove structure, we use a free-standing asymmetric trapezoidal structure cut from a film of Au on a substrate of glass.

Research conducted by former project participants[21] investigated and presented the motivation for our choice of this trapezoidal configuration. Desirable characteristics include a surface plasmon resonance within the 400-1100 nm band of solar light so that we could investigate its use of the optical solar spectrum for satellite propulsion. The geometry also needed to create a gradient optoelectromagnetic force field along the length of the nano-unit so that particle ejection could be investigated. The choice of this configuration was also motivated by the desire to obtain two dimensional precision in the direction that the nanoparticles are expelled rather than the one dimensional ejection of Shalin's group. Furthermore, fabrication of free-standing structures from a Au film on a substrate is reasonably accomplished by use of a focused ion beam (FIB).

The nanostructures are grouped by two's into a nano-unit. Each nano-unit, Figure 2.1, is a set of two asymmetric trapezoidal nanostructures where $w = 100$ nm, $l = 400$ nm, and $g = 50$ nm.

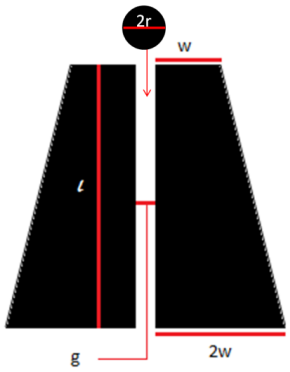

Figure 2.1: Geometry of a nano-unit comprised of two trapezoidal nanostructures.

The geometrical dimensions were chosen such that the nanostructures would resonate with a small, tunable range of incident light that is polarized perpendicularly to

their nanoparticle acceleration axis (i.e. polarized along the width of the nano-unit). Utilizing these nanostructures for satellite propulsion is achieved by the plasmonic force propulsion concept which is illustrated in Figure 2.2. A lens (not shown) is used to focus sunlight onto subwavelength metallic nanostructures that are fabricated to resonantly interact and couple with the incident light which excites surface plasmon polaritons (SPP's) on the metallic nanostructures. The SPP's generate a non-uniform electromagnetic force field that causes nanoparticles to be accelerated and expelled from the propulsion device. The nanostructures are attached to the smallsat and the non-uniform field is coupled to the nanostructures by the SPP light-matter interaction, therefore the accelerating nanoparticle propellant creates thrust by momentum exchange with the device.

Careful examination of Figure 2.2 reveals a major benefit of plasmonic propulsion: little electric spacecraft power is required. This has distinct advantages for the mass and power budget of a spacecraft, especially nanosats where mass and power are already severely limited. However, unlike other direct energy conversion propulsion technologies, plasmonic propulsion is not due to photon pressure, but rather the strong gradient optical force field generated by surface plasmon polaritons excited in the designed metallic nanostructures by the strongly resonant light-matter interaction. Specifications for a conceptual design of a plasmonic accelerator that has 35 layers, 86 array columns, multi-stage length of 5 mm, a 5-cm-diameter light focusing lens, and uses 100 nm polystyrene nanoparticles expelled at a rate of $1x10^6$ per sec would have a thrust of 250 nN, specific impulse of 10 sec, and minimum impulse bit of 50 pN-s. The thruster mass and volume are estimated at 100 g and 50 cm^3, respectively. [21] A major assumption

made for these preliminary results was the rate at which the nanoparticles are expelled, namely, f = $1x10^6$ per sec.

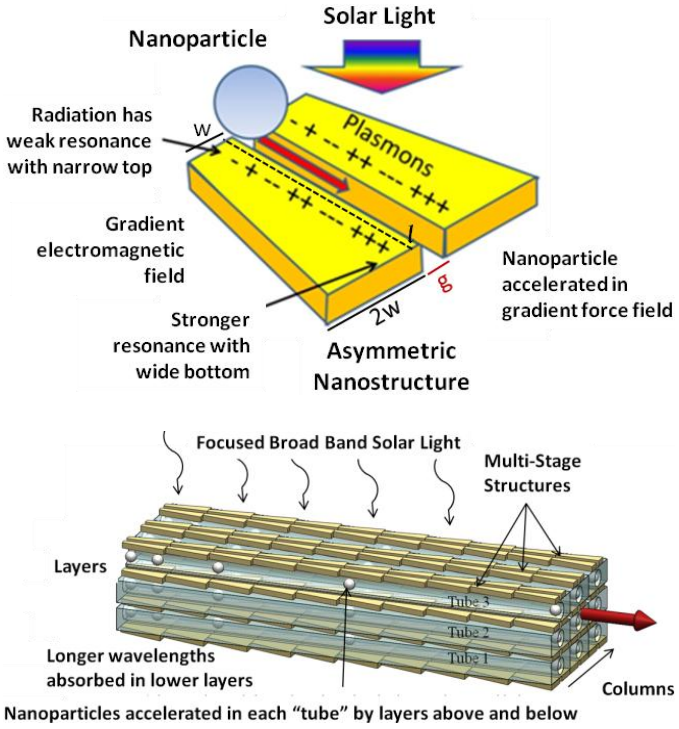

Figure 2.2: Plasmon force propulsion concept.

Photon momentum is normally too small to have any usable effect, but in nanoscale structures the transfer of linear momentum between light and matter can be greatly enhanced. Surface plasmon polaritons (SPPs) confine the electromagnetic waves into a subwavelength scale. Such a strong optical confinement results in significantly enhanced optical field strength and gradient of the light field. The finite-element analysis method (FEM) is used to calculate the optical force generated by the nanostructure.

The coupling strength determines the optical energy concentration, and is related to the gradient optical force generated by the nanostructures. This can be calculated by

integrating Maxwell's stress tensor around any arbitrary surface enclosing the nanostructure. The total gradient optical force on the charges in nanoparticle volume V is:

$$F = \int_v (E + v \times B)\rho d\tau = \int_v (\rho E + J \times B)d\tau. \quad (3)$$

The force per unit volume is

$$f = \rho E + J \times B. \quad (4)$$

eliminating ρ and J by using Maxwell's equations:

$$f = \epsilon_0(\nabla \cdot E)E + (\frac{1}{\mu_0}\nabla \times B - \epsilon_0 \frac{\partial E}{\partial t}) \times B. \quad (5)$$

Now

$$\frac{\partial}{\partial t}(E \times B) = \left(\frac{\partial E}{\partial t} \times B\right) + (E \times \frac{\partial B}{\partial t}). \quad (6)$$

According to Faraday's laws

$$\frac{\partial B}{\partial t} = -\nabla \times E. \quad (7)$$

So

$$\frac{\partial \mathrm{E}}{\partial \mathrm{t}} \times \mathrm{B} = \frac{\partial}{\partial \mathrm{t}}(\mathrm{E} \times \mathrm{B}) + \mathrm{E} \times (\nabla \times \mathrm{E}). \quad (8)$$

Thus

$$\mathrm{f} = \epsilon_0[(\nabla \cdot \mathrm{E})\mathrm{E} - \mathrm{E} \times (\nabla \times \mathrm{E})] + \frac{1}{\mu_0}\left[\mathrm{B} \times (\nabla \times \mathrm{B}) - \epsilon_0 \frac{\partial}{\partial \mathrm{t}}(\mathrm{E} \times \mathrm{B})\right]. \quad (9)$$

Which can be simplified into the Maxwell stress tensor.

$$\mathrm{T_{ij}} \equiv \in_0 \left(\mathrm{E_i E_j} - \frac{1}{2}\delta_{\mathrm{ij}}\mathrm{E}^2\right) + \frac{1}{\mu_0}\left(\mathrm{B_i B_j} - \frac{1}{2}\delta_{\mathrm{ij}}\mathrm{B}^2\right). \quad (10)$$

The indices i and j refer to the coordinates x, y and z. The stress tensor has a total of nine components (T_{xx}, T_{yy}, T_{xz}, T_{yx}, and so on). δ_{ij} is the Kronecker delta. Using Eqn. (9), the optical gradient force is calculated for asymmetric trapezoidal nanostructures subjected to light from the solar spectrum from 400 to 1100 nm.

The following sections describe theoretical and experimental studies to investigate the optical characteristics of nanostructures for plasmonic force propulsion. This is the first experiment ever attempted and first to successfully demonstrate the optical resonance of these asymmetric nanostructures. Also described are the manufacture of asymmetric nanostructures, their optical characterization, and comparison of experimental results with the numerical simulations. Specifically the experimental and numerical optical transmission spectra are compared. Results show that simulations accurately predict the wavelength of strongest resonance but they do not capture the off-

resonance behavior. Additionally we present a material and thermal analysis of nanostructures subjected to solar light to predict the maximum equilibrium temperature of nanostructures for plasmonic space propulsion.

2.2. METHODS

The finite element simulation software COMSOL Multiphysics (v. 5.0) was used to develop a three-dimensional, full-wave simulation of an array of trapezoidal nanostructures, Figure 2.3. The simulation domain size is set to be one period, 800 nm, with the thickness of the glass substrate and the air superstrate as 1.0 μm and 1.5 μm, respectively. Floquet periodic boundary conditions are applied on the four boundaries perpendicular to the structure plane due to the periodic distribution of the nano-unit structures on that plane. The top and bottom capping layers are set as perfectly matched layers (PML). A pair of ports is activated on the two PML surfaces adjacent to the

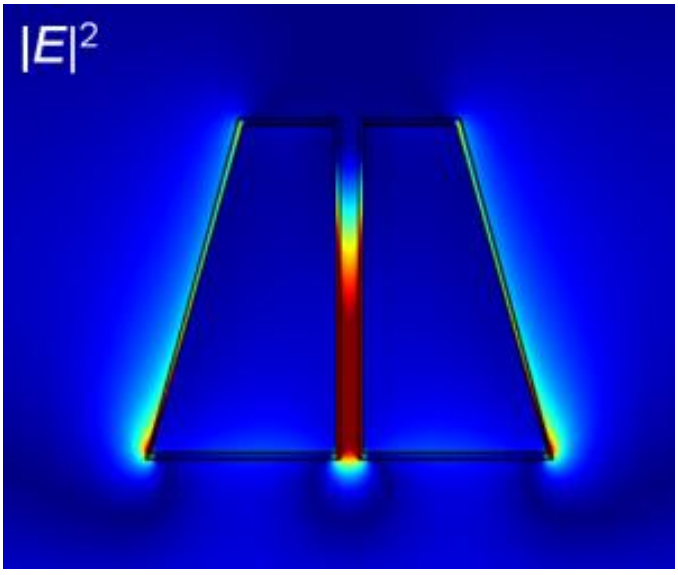

Figure 2.3: COMSOL multiphysics simulation of solar light excitation of asymmetric nano-unit.

simulation domain. The upper port serves as the plane wave light source and the other measures the transmitted electromagnetic wave. The PML condition ensures no backscattering from the two capping layers.

The computed transmission spectrum for a nano-unit, with the dimensions given in Figure 2.1, is displayed in Figure 2.4 where we can see that two peaks occur approximately at 770 nm and 845 nm. It was assumed that the nano-unit was irradiated with horizontally polarized light, or light polarized along the width of the nano-unit. The red-shaded box in Figure 2.4 indicates the wavelengths over which we can gather experimental data with our experimental equipment.

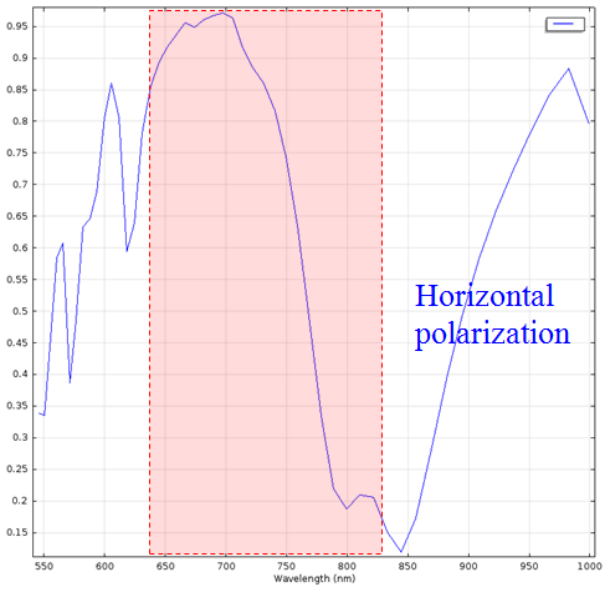

Figure 2.4: Computed transmission spectrum of the nano-units.

Using the COMSOL model of the nano-unit array, we developed an estimate of the force produced by a single nano-unit due to the optical-plasmonic interaction. Figure 2.5 shows the force profile on a glass nanoparticle as a function of position for a single

nano-unit in the array. Examination of this figure shows that the force profile extends a great distance beyond the nano-unit. Force profiles like Figure 2.5 are coupled with an array and thruster model to predict propulsion performance. The following sections describe an experimental study to investigate the optical characteristics of nanostructures for plasmonic force propulsion.

2.2.1. Fabrication. The nano-unit described in Figure 2.1 was replicated to form a repeating array. The sample that the repeating array was milled from was a thin film of

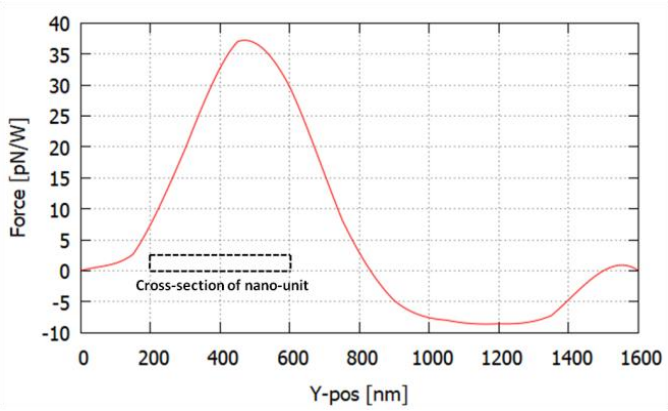

Figure 2.5: The calculated optical force profile of the nano-unit resonating near a wavelength of 770 nm.

Au, approximately 30 nm thick, deposited on a glass substrate. The focused ion beam (FIB) on the FEI Helios Nanolab 600 Dualbeam SEM/FIB was used to mill the negative area of the pattern and leave behind the freestanding nanostructures. Many parameters were altered to determine the operating conditions that produced an array of structures that had the best fit to the theoretical template. A high accelerating voltage (30 kV) was combined with a low beam current (9.7 pA) so that each gallium ion from the beam would have enough energy to mill away the sample but there would be few enough ions

hitting the sample that the pattern to be milled would not become washed out. The ion beam has a specific focal point measured to the center of the image area. As the beam moves to the edges of the image area, the beam strikes the sample at an increasingly non-perpendicular value. This change in incident angle increases the distance from the exit point of the beam at the column to the impact point of the beam on the sample surface. Therefore the beam can become out-of-focus at the edges of an image even if dynamic focus is used. A beam that is out-of-focus will produce patterns that are very low quality; the error of the manufactured pattern in relation to the theoretical template will be large. This effect can also occur if fabrication of too large an array is attempted. To stymie this, a large array of 50x50 nano-units was constructed by sequentially milling sets of 10x10 arrays adjacent to each other. Fabrication of a large array of 50x50 nano-units was necessary so that the physical dimensions of the entire array would be comparable to the optical beam that was used to experimentally determine the resonant wavelength of the array.

A good quality SEM image is one in which the features are distinguishable, specifically any edges in the image, and one in which it is in focus. This is true for FIB patterns and SEM images as well. A high-quality run of fabrication with the FIB produces patterns that have distinguishable features and are not washed out, which is caused by having a poorly focused FIB. The progression of quality of our fabricated patterns shows evidence of the improvement in the fabrication process (Figure 2.6). Focusing the FIB can be difficult because to focus the beam it must be on but when the beam is on, even at a low ion current, it causes damage to the sample. Experience in focusing the beam quickly but sufficiently is necessary.

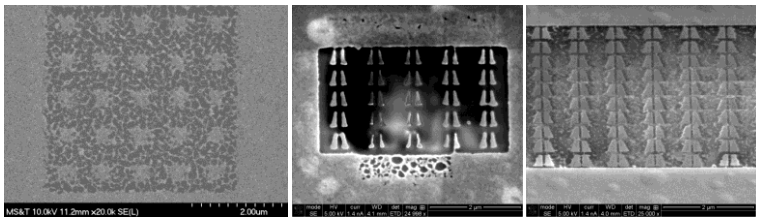

Figure 2.6: Quality progression (left to right) of array fabrication.

A 50x50 nano-unit array (Figure 2.7), with the dimensions described in Figure 2.1, and an inter-nano-unit spacing of 50 nm gives an overall array dimension of 24 μm by 22.5 μm. A subsection of this array, which was also used for optical characterization, is pictured in Figure 2.8.

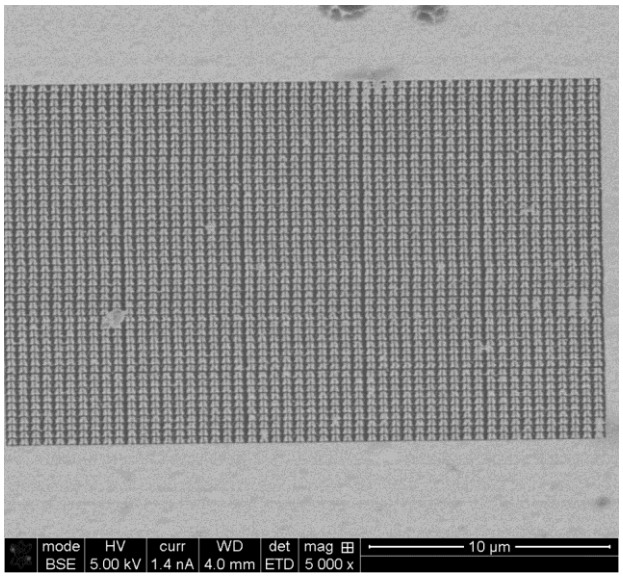

Figure 2.7: Image of the 50x50 nano-unit array.

Fabricated nanostructures were compared with the theoretically desired nanostructure array pattern to determine the array that had the least amount of error between the template and the manufactured sample. Images of each array were taken

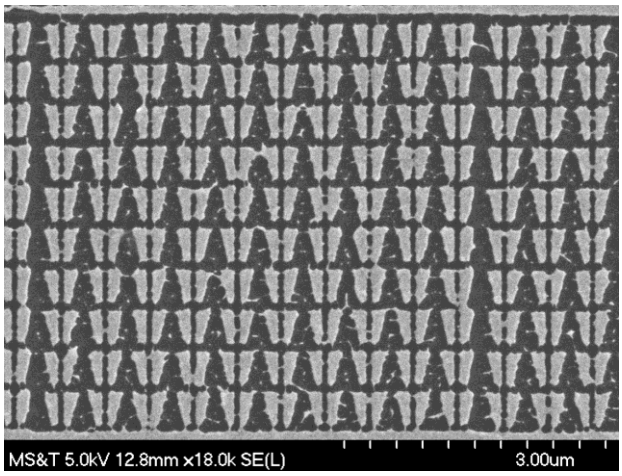

Figure 2.8: Subsection of the 50x50 nano-unit array used for optical characterization.

using the scanning electron microscope (SEM) on the above FEI system. Due to the glass substrate, heavy charging occurred throughout the array after milling took place, therefore steps were taken to reduce charging. Copper tape was attached from the gold film to the pin stub that held the sample and images were taken using backscattered electrons rather than secondary electrons. A large negative bias voltage (-150 V) was placed on the Everhart-Thornley detector so that only backscattered electrons, which have the energy of the beam, were detected. Since backscattered electrons have such high energy, the observed charging effects of the sample were minimal, if not inconsequential. Obtaining images of an array allowed each nanostructure to be measured and the roughness, a measure of the variation of each data point along an edge from its expected value, to be calculated. The approximate edge of each nanostructure was determined by finding the greatest change in pixel value of the image at the location of the nanostructure edge within the image. Then the dimensions of the nanostructures were determined by using the approximate edges that were found. The error, or roughness, along each edge of

the nanostructures was determined by calculating the distance between the approximate edge and where the edge should be. The sum of these values was then taken using the Mean Absolute Error: Eqn. (11).

$$\mathrm{MAE} = \frac{1}{n}\sum_{i=1}^{n}|f_i - y_i|. \tag{11}$$

A set of operating conditions that produced the highest accuracy nanostructures was then chosen by minimizing the roughness of the edges of the nanostructures. Using Eqn. (11), we were able to track the error for each set of operating conditions in the fabrication process. Figure 2.9 displays the error between the fabricated array and the model versus the type of electron detector used.

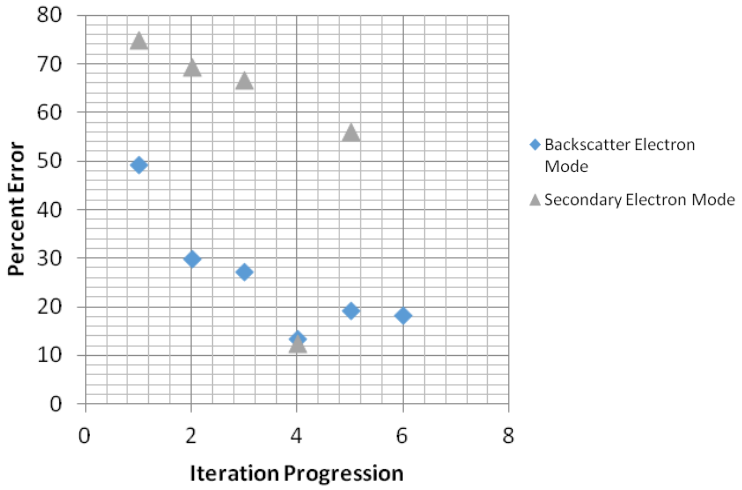

Figure 2.9: Observed error using different detection modes.

There are primarily two types of electrons that can be detected once they have interacted with the sample: 1) a backscattered electron and 2) a secondary electron. A

backscattered electron is an electron that originated from the beam and has been deflected by an angle greater than 90° out of the sample. This type of electron maintains the energy it had from the beam (5 – 30 kV) therefore any accumulated surface charge on the sample will have little effect on it. A secondary electron is an electron that has been excited and ejected from the sample. It has a much lower energy (100's of eV max) and is therefore greatly affected by any sample charge accumulation. A mixed mode detector gathers data from both types of electrons while a backscatter electron detector and a secondary electron detector primarily register their respective electrons. If Figure 2.9, we see that high observed error accompanies the use of the secondary electron mode. This is expected due to the ease at which a secondary electron is affected by accumulated sample charge. When affected by sample charging, the secondary electrons can cause image streaking, mirror effect (where incident electrons are reflected by accumulated charge rather than the sample surface) and even sample drift. These possibilities lead us to the conclusion that the use of a backscatter electron detector would be more accurate, which is supported by the data in Figure 2.9 and the images in Figure 2.10.

It was difficult to determine how each parameter affected the quality of the fabricated structures because the resolution, or quality of focus, of the ion beam when undergoing fabrication was, by far, the deciding factor. If the focus was poor, then structures like those in the first image of Figure 2.6 were created whereas those in the last image were made if the focus was tuned precisely. This factor is difficult to quantify due to its dependence on the operator. Even though the resolution of the ion beam was the predominant influence on the quality of the nanostructures, the influence of other variables on the nanostructure quality were tracked as well. Figure 2.11 shows the

percent error as it depends on the electron beam current. We would expect that the larger beam current of 10 µA would cause heavy sample charging rather than the 1.4 nA current

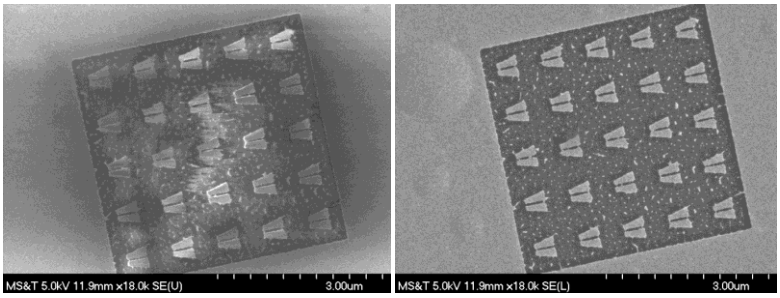

Figure 2.10: SEM images of nano-unit array (left) acquired using secondary electron detector, and (right) backscatter electron detector. Mild sample charging and image streaking are observed near the upper right of the left image.

but we suspect that the higher energy backscattered electrons overcame any charging effects in the 10 µA beam current case and conclude that data accumulation of a broader range of beam currents with each detection method is necessary for further comparison.

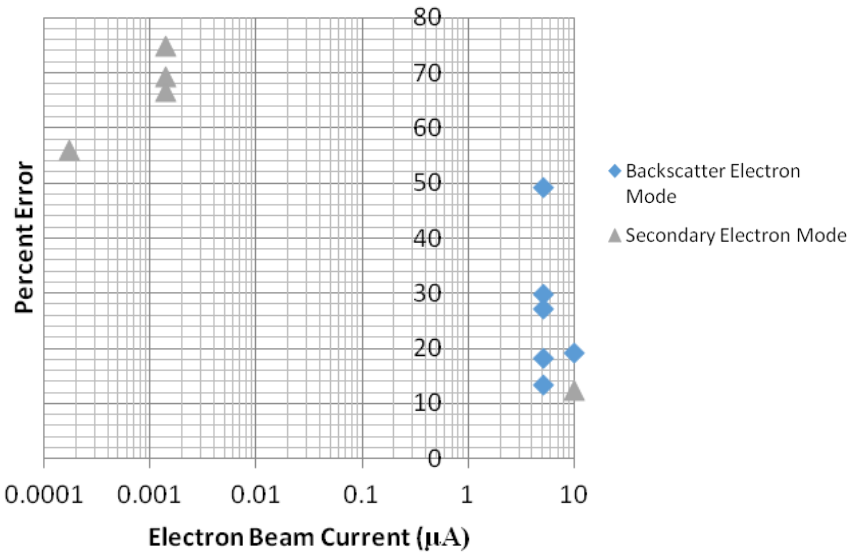

Figure 2.11: Observed error as the e-beam current varied for different detection modes.

2.2.2. Optical Characterization. The optical characterization was performed using an incoherent, Halogen, horizontally polarized, white-light source focused onto the array through a microscope to mimic solar light. Additionally, a Horiba spectrometer with a CCD detector was used to measure the intensity of light transmitted through the array. The spectrometer was used to scan through the wavelengths produced by the source to measure the transmission of the source light through the fabricated array.

Figure 2.12 (b) shows the numerical simulation and experimental results of the optical characterization of the array, normalized to the intensity of the unobstructed beam. The shaded grey region indicates the measurement error associated with the data points (the black, solid line) of the experimental characterization.

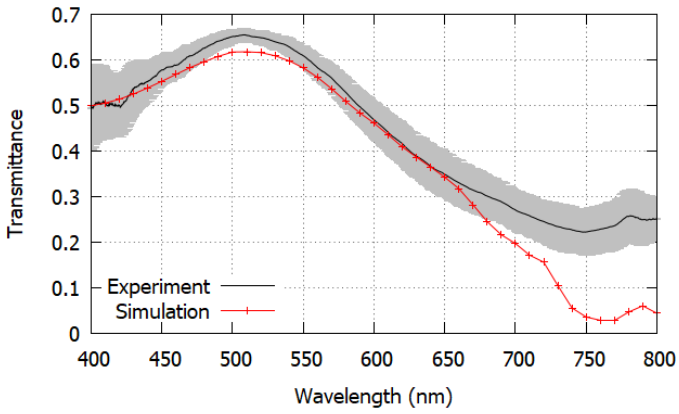

Figure 2.12: Comparison of experimental and numerical simulation results of the optical characterization.

For the experimental characterization, the resonance wavelength is 750.0 ± 0.2 nm for horizontally polarized light, and for the numerical simulation it is 770 ± 10 nm, which results in a difference of 2.6 %. The difference in resonance location is due to the error in nanostructure dimensions between the modeled nano-unit and the experimentally

fabricated nano-unit because the surface plasmon resonance is size dependent.[22,23] Figure 2.12 also shows that the transmittance of the experimental sample is 7.7 times greater than the numerical simulation at the respective resonance wavelengths. This means that less energy is absorbed by the nano-units at the resonance location than predicted by the simulation which is due to dispersion in the dimensions of the nano-units within a single array. Mock, et. al.[23] shows that a change in nanostructure shape from a triangle of side length 83 nm to approximately the same size pentagon or sphere causes the peak plasmon resonance wavelength to shift by 110 nm and 150 nm, respectively. Therefore, variations in shape between nano-units cause the resonance location for each nano-unit to shift in relation to each other. At the desired resonance location there are fewer nano-units within the array that are absorbing the incident light, which allows a higher percentage of the incident light to transmit through the array at the desired resonance location.[22,23] This implies that as the uniformity of the nano-units increases, the resonance of the array at a single location will also increase and that the resonance peak will narrow. We see that the overall shape of the transmittance spectra of the numerical simulation and the experimental characterization agree over the entire spectrum, even off-resonance.

2.2.3. Dynamic Excitation. The potential profile computed for the nano-unit assembly, Figure 2.13, was revisited and analysis lead to the conclusion that the profile is a potential well that returns to zero. This follows from a simple understanding of the conservation of energy that any potential must return to zero at an infinite distance from the source. Therefore, constant irradiation as initially envisioned would cause trapping of the nanoparticles rather than acceleration and expulsion. This led us to develop and investigate other theories to accelerate the nanoparticles away from the plasmonic

nanostructures. One possible way to accelerate and expel nanoparticles is to pulse the light source, that is, to provide dynamic excitation to the nanostructures. With constant light source, trapping would occur in a location off-center in relation to the nano-unit which may prove to be useful in other applications but, in this instance, acceleration is the preferred response.

The dynamic excitation theory maintains a constant pulse length of the incident light, both the on and off modes, and changes the path length of each acceleration stage so that one light pulse can synchronously accelerate each nanoparticle located at every acceleration stage. The main question we seek to address in investigating this theory is whether or not the total length of the assembly will be reasonably scaled for the application as a propulsion device for smallsats. We answer this question by calculating the total length it would take for a nanoparticle to be accelerated from rest to 1 m/s.

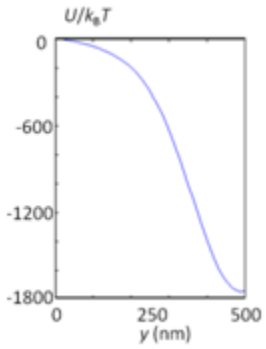

Figure 2.13: Potential profile of a nano-unit.

If the incident light is pulsed in a way that allows the nanoparticle to initially accelerate down the potential in Figure 2.13 then travel at a constant velocity away from the structure when the nanoparticle reaches the minimum of the well, the nanoparticle

may not feel a force acting against its motion and can be expelled as propellant. This will occur if the light pulse irradiates the nano-unit while the nanoparticle travels the distance from the start of the potential well to the minimum of the well then the pulse turns off while the nanoparticle travels the distance to the beginning of the potential of the next nano-unit in a multistage array. When the light pulse is on, the nanoparticle feels a force that pulls it towards the minimum of the potential well but when the pulse is turned off the potential well is destroyed and the nanoparticle no longer feels a force from it; therefore it continues in motion under constant velocity. As the nanoparticle proceeds through progressive stages of acceleration its velocity increases, this means that the distance the particle travels while the light beam is off must also increase so that the timing of the light pulse can remain constant. If the pulse width of the light beam was altered rather than the separation distance between acceleration stages, nanoparticles would be out of phase with each other when they arrived at new acceleration stages such that that when the light pulse turned on to accelerate one nanoparticle it would hinder the motion of another nanoparticle because the second nanoparticle may not be in the constructive acceleration zone of an acceleration stage.

The dynamic excitation model calculates the amount of acceleration that a nanoparticle would feel from a single nano-unit stage. This acceleration value will be the same for each stage, therefore we can 1) calculate the exit velocity of a nanoparticle from a single stage, 2) use this velocity to determine the distance the nanoparticle travels while the light pulse is off, 3) also use this velocity as the initial velocity into the next acceleration stage, and 4) iterate this process until the desired velocity is obtained. Then we can review the device parameters that are required to achieve that velocity such as the

total length of the device and the number of nano-unit stages needed to accelerate the nanoparticles to the desired velocity.

The actual force generated by the nano-unit acting on the nanoparticles can be determined from the repulsive force profile in Figure 2.5: The calculated optical force profile of the nano-unit resonating near a wavelength of 770 nm. (where force generated by the nano-unit is given per Watt) and Eqn. (14), by factoring in how many total Watts the nano-unit absorbs at its resonance frequency. Say, there is incident light, representative of solar radiation, of $I_{leo}\ \frac{kW}{m^2}$. Then the energy absorbed by the nano-unit is given by Eqn. (13), where its cross-sectional area is found in Eqn. (12) and the area of the light capturing lens is known.

$$A_{nano} = 2 * \left(\frac{b_1 - b_2}{2} h\right). \tag{12}$$

$$P_{nano} = P_{image} \frac{A_{ns}}{A_{image}} = I_{leo} \frac{A_{lens} A_{nano}}{A_{image}}. \tag{13}$$

$$\vec{F}_{nano} = \vec{F} * P_{nano}. \tag{14}$$

$$\vec{a}_{nano} \Delta x_a = \frac{\vec{F}_{nano}}{m} \Delta x_a = \int \frac{\vec{F}}{m} dx. \tag{15}$$

The change in velocity of the nanoparticle due to one nano-unit can be determined by dividing the actual force by the mass of the nanoparticle, which was determined from the volume of a polystyrene nanosphere with radius r = 50 nm. If the nanoparticle has no

initial velocity, then the velocity it has after passing over one asymmetric nano-unit is given by Eqn. (16).

$$v_{f_1} = \sqrt{2a_{nano}\Delta x_a}. \tag{16}$$

Eqn. (16) is studied in plots (a) and (b) of Figure 2.14 where a parametric sweep is performed on the length of the plasmonic nano-units (h = 200 nm – 10.0 μm), the radius of the light absorbing lens (5.0 mm – 50.0 cm), and the intensity of the solar irradiance in low Earth orbit (0.5 W – 1.5 kW). Throughout this parametric sweep, Eqn. (15), the acceleration from a single nano-unit stage times the distance of that stage, is assumed to remain constant. In Figure 2.14 (a) and (b), we see that the final velocity of a

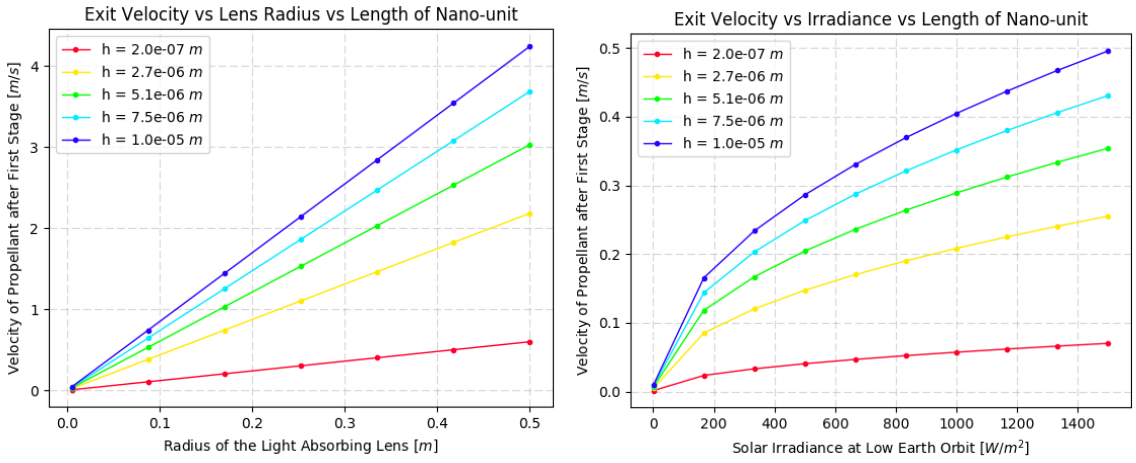

Figure 2.14: Particle velocity at exit of first stage as it depends on the length of the nano-unit, the light capturing lens radius, and the solar irradiance.

particle after it has passed by a single acceleration stage of the PFP thruster increases with respect to each of the parameters stated above. This is reasonable because all three

parameters describe a change in the amount of energy absorbed by the nano-units from the incident solar radiation. As the length of the nano-unit increases its light-absorbing cross-sectional area also increases. As the lens radius increases, its light-collecting cross-section increases and the optical energy density at the focus of the lens increases. Also, it is trivial to say that as the solar irradiance increases, the energy delivered to the system also increases. Figure 2.15 shows that the nanoparticle experiences diminishing returns as its velocity increases, such that a larger distance and increasing iterations of nano-units must be met to gain equivalent increases in velocity.

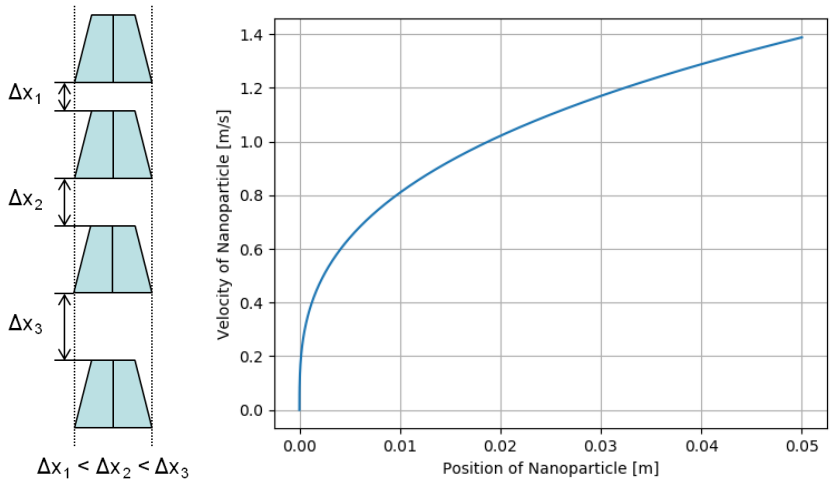

Figure 2.15: Velocity of nanoparticle as its position increases.

Let $I_{leo} \sim 1\frac{W}{m^2}$ at a wavelength of 800 nm, the approximate resonant wavelength of the test structure. Also, let $A_{nano} = 1.2 * 10^{-13} m^2$ and $R_{lens} = 5\,cm$ so that $a_{nano} = 9.84 * 10^{-3}\ \frac{m}{s^2}$ and $v_{f_1} = 1.28 * 10^{-4}\ \frac{m}{s}$ with Δx = 831 nm. We can now choose a shutter speed for the light pulse such that the incident light beam is blocked while the nanoparticle travels between nano-units. Using the above values and computationally

iterating the motion and velocity of the nanoparticle, the acceleration length of the system can be determined, Figure 2.15.

With a shutter speed of $t_{sh} = 0.1\,\text{ms}$, it takes the nanoparticle 27.4 μm to accelerate 0 m/s to ~10 cm/s but it takes 16.4 mm for the nanoparticle to double its speed from ~10 cm/s to ~20 cm/s. For the nanoparticle to reach a velocity of 1 m/s, it takes a total acceleration path length of 1.88 cm. To remedy the trapping attribute of the nano-units when held under constant illumination a pulsed beam of incident light was considered. This method shows promise because an appreciable particle velocity of 1 m/s is achievable within 1.88 cm. Though the acceleration path length of the thruster will need to be lengthened, from the aforementioned 5 mm, this new path length of ~2 cm is still a reasonable size for a small-satellite thruster.

2.2.4. Material Analysis. In the field of nanoparticle manipulation, semi-conductors offer striking benefits over metals in the near infrared and optical frequency range because they experience lower losses[24] and increased tunability[25]. Semiconductors have been coupled with plasmonic antennas in configurations such as Abb, et al.'s Au-ITO hybrid system that enables ultrafast nanoplasmonic switching.[26] More recently plasmonic semiconductors, such as ITO, have been used in ambient air as high-efficiency thermal emitters[27]. Compared to metal, semiconductor nanostructures may provide stronger electric fields for nanoparticle manipulation and injection systems. Further, they may also provide enhanced thermal stability. In order to investigate the potential benefits and enhancement provided by semiconductor nanostructures, we explore the effects of semiconductors, such as gallium arsenide (GaAs), indium tin oxide (ITO), and aluminum zinc oxide (AZO), on the electromagnetic response of a set of two asymmetric

trapezoidal nanostructures, as shown in Figure 2.1. We also investigate the thermal stability of semiconductor nanostructures compared to metal by developing a model for the nanostructure equilibrium temperature when subjected to various radiation intensities.

The dielectric function of a material governs how it responds to incident electromagnetic radiation. Eldlio, et al. proposes[28] that the combination Drude-Lorentz model works well to describe the dielectric function of a semiconductor. The Drude model is a classical description of the optical response of metals and treats the atomic valence electrons as freely moving (also known as the sea of electrons or free electron model). The Drude model, Eqn. (3), is sufficient for metals but not semiconductors because it does not capture the bound electron and hole attributes nor the spatial distribution of the dielectric constant that can be present in semiconductors. ε_∞ is the high frequency dielectric permittivity, ω_p is the plasma frequency, and γ is the damping factor. The plasma frequency is defined in Eqn. (18), where ε_0 is the permittivity of free space, n is the charge carrier density, e is the electron charge, and m^* is the effective electron mass.

$$\varepsilon_r = \varepsilon_\infty - \frac{{\omega_p}^2}{\omega(\omega+j\gamma)}. \tag{17}$$

$$\omega_p = \sqrt{\frac{ne^2}{\varepsilon_0 m^*}}. \tag{18}$$

The Lorentz model, Eqn. (19), is valid for materials with bound electrons oscillating around their parent atom. Like the Drude model, the Lorentz model is also

insufficient to fully describe the optical response of semiconductors because of its strong dependence on the resonant frequency and that it is only valid in the frequency regime in which intraband transitions do not occur. ∇_ϵ is an amplitude factor, or oscillator strength, determined by the difference between the static permittivity, ε_{st}, and the high frequency permittivity, ε_∞: $\nabla_\epsilon = \varepsilon_{st} - \varepsilon_\infty$. The static permittivity of a semiconductor is measurable when the material is undoped. ω_0 is the resonant frequency of the charge carriers and is equivalent to the band gap energy in a semiconductor. The Lorentz model makes use of the analogy between a bound electron and an oscillator (Lorentz oscillator) to model the system with an associated resonant frequency.

$$\varepsilon_r = \varepsilon_\infty + \frac{\nabla_\epsilon {\omega_p}^2}{-\omega^2 + j\gamma\omega + \omega_0}. \tag{19}$$

The Drude-Lorentz model is a linear combination of the constituent models, as shown in Eqn. (20), and provides a better description of the dielectric permittivity of a material because it can effectively couple the contributions from interband (bound-electron) and intraband (free electron) effects which are present in a semiconductor. This combined description was used to define material response in our computational models.

$$\varepsilon_r = \varepsilon_\infty - \frac{{\omega_p}^2}{\omega(\omega + j\gamma)} + \frac{\nabla_\epsilon {\omega_p}^2}{-\omega^2 + j\gamma\omega + \omega_0}. \tag{20}$$

Again, COMSOL Multiphysics modeling software was used to develop a numerical three-dimensional, finite element, full-wave analysis of the optical interaction between

incident radiation and the trapezoidal nanostructures. Floquet periodic boundary conditions were applied on the four boundaries perpendicular to the plane of the structure in order to model a periodic distribution of the nano-unit structures. The top and bottom capping layers were set as perfectly matched layers (PML) to ensure no backscattering from the boundary. A port was specified above the nanostructures to indicate the inlet for the incident radiation and was polarized along the width, w, of the nanostructures. Material composition was controlled by specifying the variables in the Drude-Lorentz model. The parameters used in the model are tabulated below in Table 2.1.

Table 2.1: Specified parameters for the Drude-Lorentz model for each material studied.

	Au[29,30]	GaAs[31-34]	ITO[35,36]	AZO[37-39]
Oscillator Strength, ∇_ϵ	0.94	2.01	3.781	7.93
Resonance Freq., ω_0	4.03e15 rad/s	2.93e7 rad/s	7.02e15 rad/s	5.12e15 rad/s
Plasma Freq., ω_p	2.15e15 rad/s	2.13e11 rad/s	1.14e15 rad/s	1.2e15 rad/s
High Freq. Permittivity, ε_∞	1.53	10.89	4.00	2.97
Static Permittivity, ε_{st}	2.47	12.9	7.78	10.9
Damping Term, γ	17.1e12 rad/s	2.60e13 rad/s	7.10e14 rad/s	6.25e13 rad/s
Charger Carrier Density, n	5.9e22 $1/cm^3$	1e18 $1/cm^3$	6.64e20 $1/cm^3$	1.13e20 $1/cm^3$

Figure 2.16 shows, as an example, the GaAs asymmetric nanostructure in the COMSOL software interacting with light at a wavelength of 540 nm. The color plot indicates the profile of the magnitude of the electric field in the y-direction. The electric field in the gap between the two nanostructures is computed and used to compare the

response of the different materials. A rectangular test area is drawn between the two nanostructures, visible in Figure 2.16 as a red-dashed rectangle, over which the average of the magnitude of the electric field in the y-direction is computed for each wavelength.

The averaged values calculated over the rectangular test area are plotted in Figure 2.17 versus wavelength for each material composition. The curve for Au shows a uniform response over the majority of the test wavelengths, leveling off at about 28 MV/m as wavelength increases. There is also a localized but distinct minimum located at approximately 450 nm that coincides with a peak in the reflectance and absorptance curves (Figure 2.18). The GaAs curve displays an overall increasing trend as the wave-

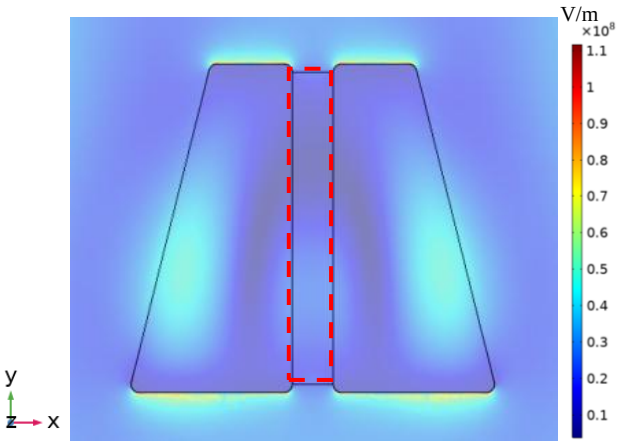

Figure 2.16: Color plot of the magnitude of the electric field in the y-direction at a wavelength of 540 nm (material: GaAs). The test volume over which the electric field is averaged is visible as a red-dashed rectangle between the nanostructures.

length increases and contains two local peaks of 14.5 MV/m and 28.1 MV/m located at approximately 540 nm and 850 nm, respectively. The ITO and AZO curves show nearly identical responses with a small peak of 28.6 MV/m at about 850 nm and an overall arch-shaped increasing trend as wavelength increases. The AZO curve does indicate a slightly

stronger field than ITO at lower wavelengths with an approximate increase of 700 kV/m at a wavelength of 600 nm from 24.4 MV/m (ITO) to 25.1 MV/m (AZO).

The reflected, transmitted, and absorbed light resulting from the interaction was also calculated and plotted as a fraction of the total incident light in Figure 2.18 (reflectance, transmittance, and absorptance; or RTA). There is a peak in the Au reflectance at approximately 465 nm and in the absorptance at approximately 470 nm that coincides with the resonance frequency value of 4.03e15 rad/s or 467 nm used in the

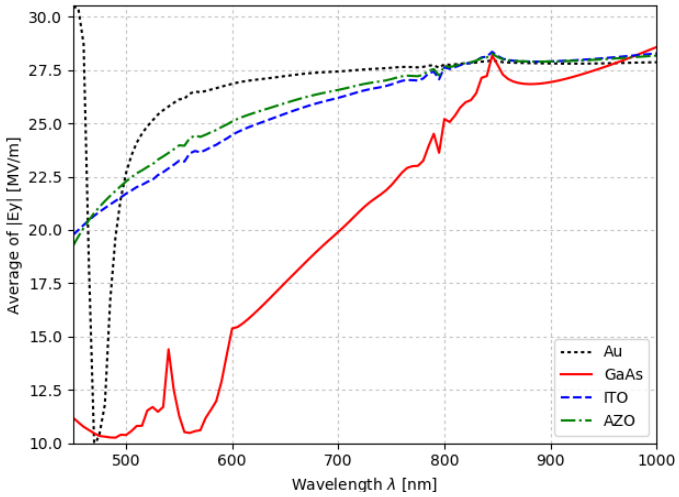

Figure 2.17: Average of the magnitude of the electric field in the y-direction, using the space within the gap as the test volume, plotted versus incident wavelength for each material composition.

Lorentz piece of the numerical model. For GaAs, the transmittance increases and the reflectance decreases with increasing wavelength. The absorptance also increases with increasing wavelength and contains a local maximum at approximately 540 nm which corresponds to the electric field produced by the nanostructures as indicated in Figure 2.17. ITO and AZO produce nearly identical responses in their calculated RTA values,

with absorptance monotonically decreasing over the range, reflectance showing a minor oscillation about the operating reflectance value of 0.038 and strong, slightly decreasing transmittance.

2.2.5. Thermodynamic Stability Analysis. Calculations to determine the equilibrium temperature of the nanostructures under incident light were also performed because the nanostructures need to be kept from melting during use; otherwise their shape would be irreparably changed and the desired asymmetric profile would be lost. The light power incident on the nano-unit is given by Eqn.(21)

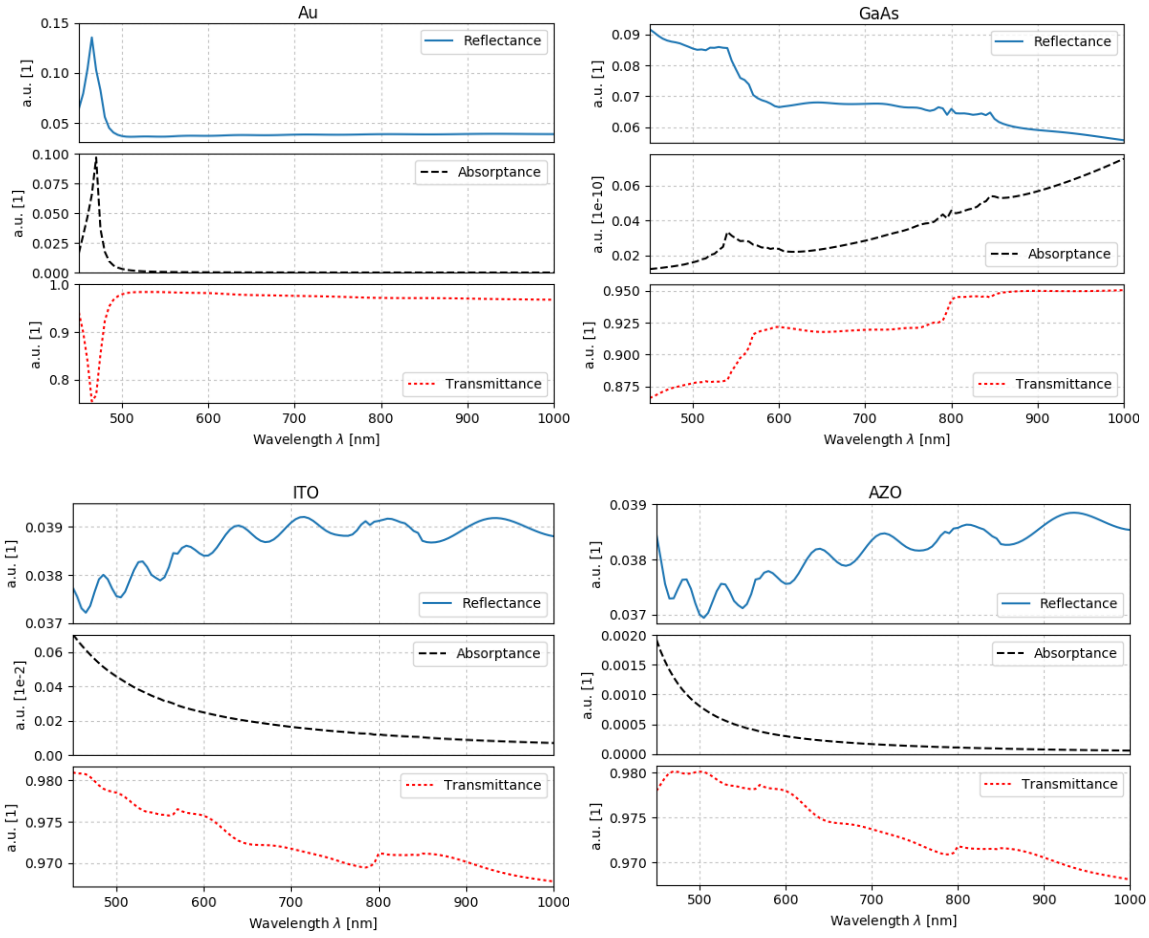

Figure 2.18: Reflectance (black dotted), transmittance (red), and absorptance (black dashed) curves for each material versus wavelength.

The nanostructure radiates and conducts energy in addition to absorbing it. Therefore, the Stefan-Boltzmann law can be used to calculate the energy radiated, Eqn. (22)(a), and the conductive heat transfer can be calculated using Eqn. (22)(b) where ε is the emissivity of the material, σ is the Stefan-Boltszmann constant, $s_{ns} = 50\ \text{nm}$ and $s_{sub} = 1500\ \text{nm}$ are the thickness of the nanostructure and substrate, respectively, and, k_{ns} and $k_{sub} = 1.4\ \frac{W}{mK}$ are the thermal conductivities of the nanostructure and substrate, respectively. T_e is the temperature of the environment, taken to be 298.15 K and T is the temperature of the material. Light intensity ranging from 0 to 2.5 GW/m^2 is used to capture the response of a wide range of lighting environments including shaded, oblique incident light angle (Figure 2.19), and laser illuminated.

$$P_{nano-unit} = IA_{nano-unit}. \tag{21}$$

$$\text{(a) } P_{rad} = \varepsilon A_{ns}\sigma\left(T^4 - {T_e}^4\right)$$
$$\text{(b) } P_{cond} = \frac{(T-T_e)A_{ns}}{\frac{s_{ns}}{k_{ns}}+\frac{s_{sub}}{k_{sub}}} \tag{22}$$

Setting the incident power equal to the sum of the Stefan-Boltzmann radiated power and the conductive heat transfer we can find the equilibrium temperature of the nanostructures. We compare the thermal response of the nanostructures when composed of different materials. The material property values are listed in Table 2.2. Figure 2.20 shows how the equilibrium temperature is dependent upon the light intensity and material composition of the nanostructures. The horizontal dashed lines indicate the bulk melting

point temperature of each material which provides an upper limit to the equilibrium temperature achievable by the nanostructures[40]. From this plot we see that the

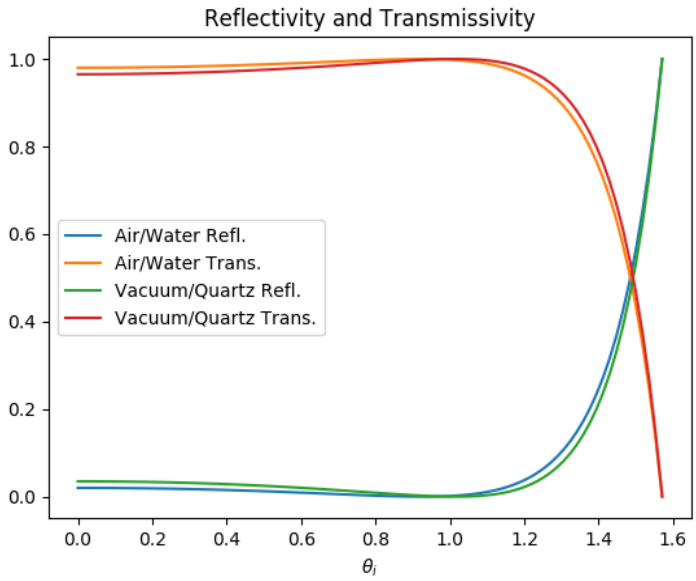

Figure 2.19: The reflected and transmitted light striking a flat surface as it depends on the incident angle, normalized to the incident radiation.

relationship is linear which implies most of the heat generated by absorbing the incident light is conducted away from the nanostructures through the substrate. We also see that

Table 2.2: The emissivity and thermal conductivity values for each material used in the equilibrium temperature analysis.

	ε	k [W/m/K]	Melting point [K]
Au	0.47	310	1337
GaAs	0.648	0.201	1513
ITO	0.25	5.86	2800
AZO	0.6	7.5	2248 (ZnO)

GaAs conducts heat the least efficiently and therefore has a higher equilibrium temperature for all incident light intensities. With the provided melting point values (with ZnO in place of AZO) we see that GaAs can interact with light intensity less than 920 MW/ m^2 without melting, Au with 969 MW/ m^2, AZO with 1.81 GW/ m^2, and ITO with 2.32 GW/ m^2.

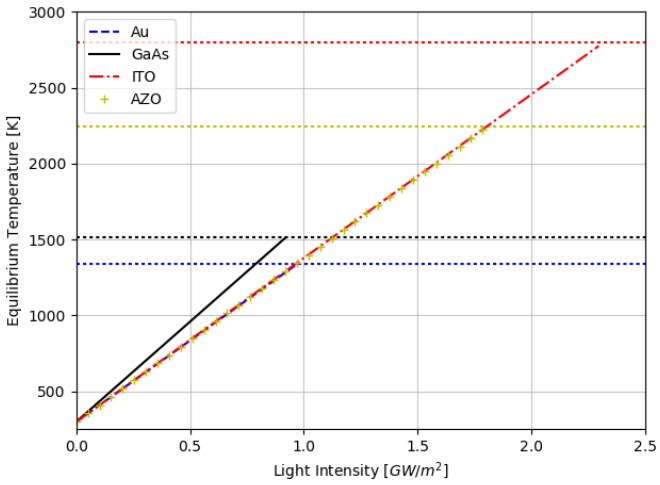

Figure 2.20: Equilibrium temperature of radiating and thermally conducting nanostructures versus a range of incident light intensity. Horizontal lines indicate the bulk melting point temperature of each material.

3. CHARGED PARTICLE/ION ACCELERATION

3.1. CHARGED ACCELERATION BACKGROUND

Particle accelerators, linear or otherwise, are in abundant use in experimentation and application. Their uses range from cancer therapy in advanced medical centers to circuit printing of computer chips and isotope production for use as radioactive tracers to crystal analysis by X-ray diffraction [6]. The vast abilities of particle accelerators make them highly desirable but their downfalls include their large physical size and the enormous cost it takes to build, run and maintain a high energy accelerator. Reducing the financial and physical footprint of particle accelerators is the primary driving force in the search for a feasible tabletop accelerator that can accelerate particles to high energies (MeV or greater).

The separation of charges in a plasma, by the propagation of a laser through that plasma, creates very strong accelerating fields that travel in a wake behind the laser [41]. The maximum accelerating field in a plasma wakefield setup is given as $E = -m\omega_p c/e \approx \sqrt{10n_0}\mathrm{Vm}^{-1}$ [6], where n_0 is the plasma density. Therefore the accelerating field can be increased by increasing the density of the plasma, this implies that an over-dense plasma such as a metal might be used as a particle accelerating mechanism. When groups of electrons in a metal are excited by incident electromagnetic radiation such that they oscillate about their equilibrium position due to the oscillating electric field of the impinging light they are called plasmon polaritons. The interest for particle acceleration lies in the surface plasmon polaritons (SPP's) which are groups of electron oscillations that are confined to, and propagate along, the surface of the metal. A plasmon linac

would harness these propagating SPP's in order to accelerate particles in the EM wakefield that they create.

Previsously in this field, Saito and Ogata[42], have investigated the theory and proposed an experimental setup to accelerate electrons using a plasmon linac wakefield accelerator. Below we investigate the theory and accelerating modes and experimental setup for ions, which have a much lower energy then electrons and therefore couple to the SPP's at a much smaller phase velocity. We perform this investigation by studying the dispersion curve of the SPP's at large wavenumber values and analyzing coupling mechanisms so that energy can be transferred from SPP's to the particles.

3.2. METHODS

The laser is incident upon the nanostructure hole array (Figure 3.1) and excites SPP's on the surface of the thin film which contains the hole array. The radius (a) of the holes is approximately that of the laser wavelength. SPP's are electromagnetic (EM) waves that are confined to 2 dimensions and are able to propagate along the inside surface of the holes because they have a shorter wavelength than the incident/exciting light of the laser.[43] The characteristic profile of the EM-field inside the holes satisfies the cylindrical Bessel function equation [44] with radial symmetry, such that [42]: for $r \leq a$

$$E_r = -\left(\frac{ik}{K_0}\right) A_0 J_1(K_0 r). \tag{23}$$

$$E_z = A_0 J_0(K_0 r). \tag{24}$$

$$B_\theta = -\left[\frac{i(K_0{}^2+k^2)}{\omega K_0}\right] A_0 J_1(K_0 r). \tag{25}$$

for $r > a$

$$E_r = -\left(\frac{ik}{K_1}\right) A_1 H_1{}^{(1)}(K_1 r). \tag{26}$$

$$E_z = A_1 H_0{}^{(1)}(K_1 r). \tag{27}$$

$$B_\theta = -\left[\frac{i(K_1{}^2+k^2)}{\omega K_1}\right] A_1 H_1{}^{(1)}(K_1 r). \tag{28}$$

The cylindrical, 1D, geometry can only support EM waves with the magnetic induction field perpendicular to the plane of incidence, a transverse magnetic field [45]. The SPP's that travel along the inside surface of the holes are frequency dependent and their

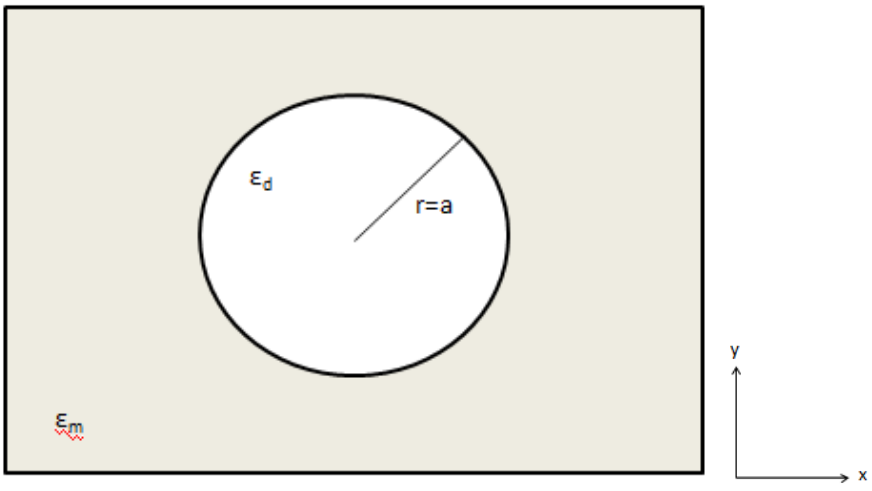

Figure 3.1: Geometry of single hole in nanohole array.

dispersion can be determined by solving Maxwell's equations at the dielectric-metal interface with appropriate boundary conditions.

At the interface within the cylindrical hole, where r = a, the longitudinal component of the electric field, in the z-direction, parallel to the surface interface, must be equal on either side of the interface (i). The magnetic induction field must be equal at the interface in the θ direction, parallel to the interface (ii). Also, in the radial direction, perpendicular to the interface, the permittivity of the metal times the electric field in it must equal the permittivity of the dielectric times the electric field in it: Eqn. (29) (iii). [46]

$$\text{(i) } E_{z,m} = E_{z,d} \quad \text{(ii) } H_{\theta,m} = H_{\theta,d} \quad \text{(iii) } \epsilon_m E_{r,m} = \epsilon_d E_{r,d}. \tag{29}$$

Eqns. (30) and (31) follow from Eqns. (24), (27), and (29)(i) and Eqns. (23), (26), and (29)(iii), respectively:

$$A_0 J_0(K_0 a) = A_1 {H_0}^{(1)}(K_1 a). \tag{30}$$

$$-\epsilon_1 ikA_1 {H_1}^{(1)}(K_1 a)/K_1 = -\epsilon_0 ikA_0 J_1(K_0 a)/K_0. \tag{31}$$

The constants A_0 and A_1 can be dropped if Eqns. (29)(i) and (29)(iii) are combined which gives the lossless dispersion of the SPP's as

$$\frac{\epsilon_0 J_1(K_0 a)}{K_0 J_0(K_0 a)} - \frac{\epsilon_1 {H_1}^{(1)}(K_1 a)}{K_1 {H_0}^{(1)}(K_1 a)} = 0. \tag{32}$$

where

$$K_i^2 = \frac{\omega^2 \epsilon_i(\omega)}{c^2} - K^2. \quad \text{for } i = 0,1. \tag{33}$$

Plotting this dispersion for a variety of $k_p a$ values gives the following graph, Figure 3.2.

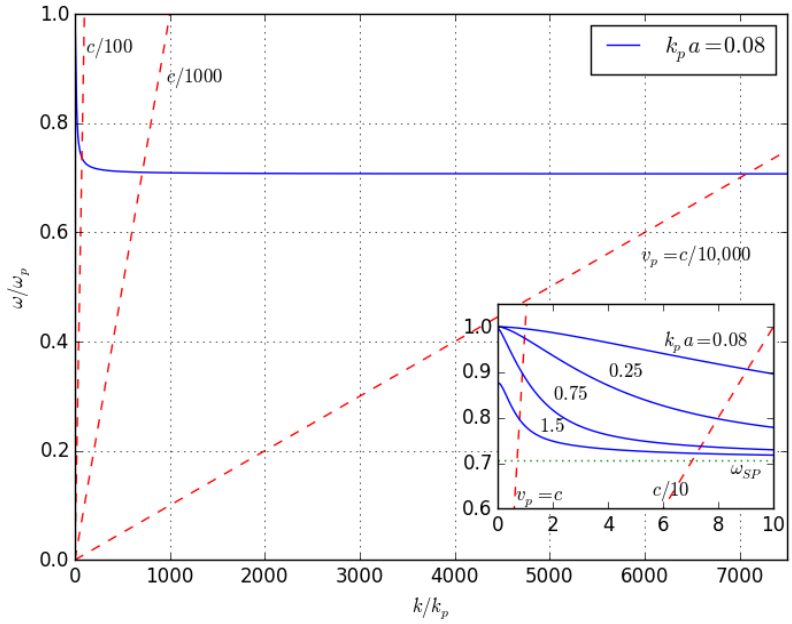

Figure 3.2: Surface plasmon polariton dispersion within cylindrical nanoholes.

3.2.1. Phase Matching in a Cylindrical Plasmon LINAC. The inset shows small values for k/k_p that correspond to particles with high velocity. The main portion of the plot shows how the SPP dispersion goes to a constant value, ω_{sp}, in the limit of large k/k_p. ω_{sp}, also designated in the inset, is the surface plasmon frequency and is equal to 0.707 ω_p when air is the dielectric, and can be analytically determined by [43] Eqn. (34). ω_p

is the characteristic plasma frequency of the metal. . This means that in the limit of large k/k_p, where slow (v << c) particles will intersect the dispersion curve, the SPP frequency

$$\omega_{sp} = \frac{\omega_p}{\sqrt{1+\epsilon_{dielectric}}} \overset{air}{\Rightarrow} \frac{\omega_p}{\sqrt{2}} = 0.707\omega_p. \tag{34}$$

can accurately be approximated as the surface plasmon frequency, ω_{sp}. This implies that the frequency of the laser used to excite the SPP's will also need to be equal to $\omega_{sp} = 0.707\omega_p$, corresponding to a wavelength of $\lambda_L = 2\pi c/.707\omega_p = 202$ nm. It is also shown in the above plot that, as the particle velocity increases due to energy transfer with the SPP's, the same laser frequency/wavelength can continue to be used to excite the SPP's because the their frequency will remain at ω_{sp}, as long as v << c. Figure 3.3 shows the $\frac{1}{x}$ relation between the k value and the particle velocity for the intersection of the SPP dispersion curve and the particle dispersion curve for particles in the range v << c.

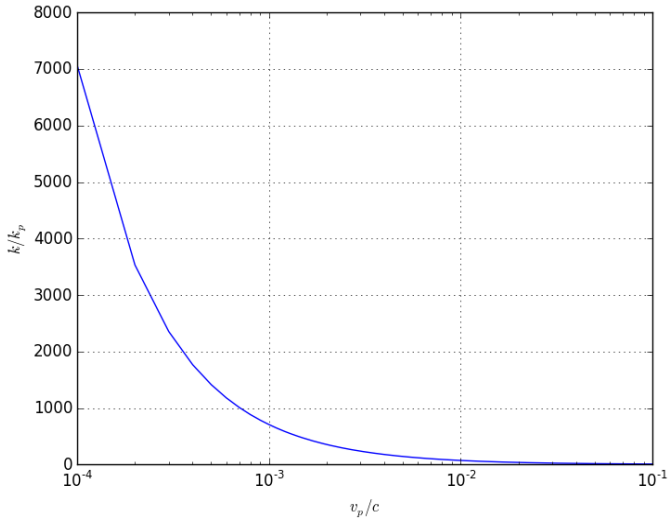

Figure 3.3: Wave number versus particle velocity.

It may be desirable to decrease the SPP limiting value to say, $\omega_{sp} = 0.5\,\omega_p$, for two specific reasons. The first is that a metal experiences a drastic decrease in its reflectivity above its plasma frequency and "…acts like a nonabsorbing transparent dielectric…" [47]. If the metal does not absorb the incident radiation then SPP's cannot be excited. The second reason is that there are only a few sources that produce laser light in the 200 nm range, such as the ArF excimer laser [48] or the "mixing after doubling" [49] experimental apparatus. Therefore, if the surface plasmon frequency is decreased to a lower percentage of the plasma frequency, the interaction between the laser and the SPP's will occur deeper into the safe region of high reflectivity and a higher wavelength laser can be used to actually excite the SPP's.

The SPP limiting value can be tuned by changing the permittivity of the dielectric within the interaction area of the nanohole, Figure 3.4. If the dielectric permittivity is 2.0, double that of air, then the surface plasmon frequency will be $\omega_{sp} = 0.577\,\omega_p$, which corresponds to a laser interaction wavelength of $\lambda_L = 240$ nm.

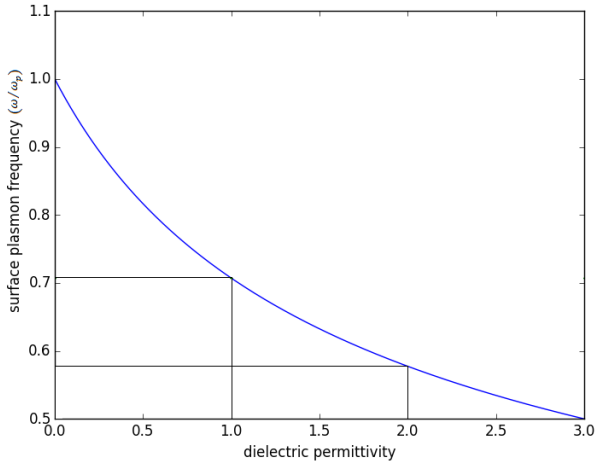

Figure 3.4: Surface plasmon polariton limiting frequency as it depends on the permittivity of the dielectric.

3.2.2. Wave-Vector Coupling. For the incident laser light to excite SPP's, the laser and the SPP's must be phase matched: their wave vectors must be matched. This is because the SPP dispersion curve lies outside the light cone of the dielectric such that the propagation constant of the SPP is greater than that of the incident light. A feasible phase matching setup for the aforementioned nanohole array is the method of grating coupling.[43] Phase matching occurs in 1D when

$$k_{sp} = \sqrt{\epsilon_0} k_L \sin\theta \pm \frac{2m\pi}{a}. \tag{35}$$

θ is the incident angle of the laser measured to the surface normal, m is an integer (1, 2, 3…) denoting the diffraction mode, and a is the lattice spacing. When a beam of light strikes the surface of a material with a high reflectivity, the light reflects off of the surface at the same angle (measured to the normal) that it struck the surface. If the

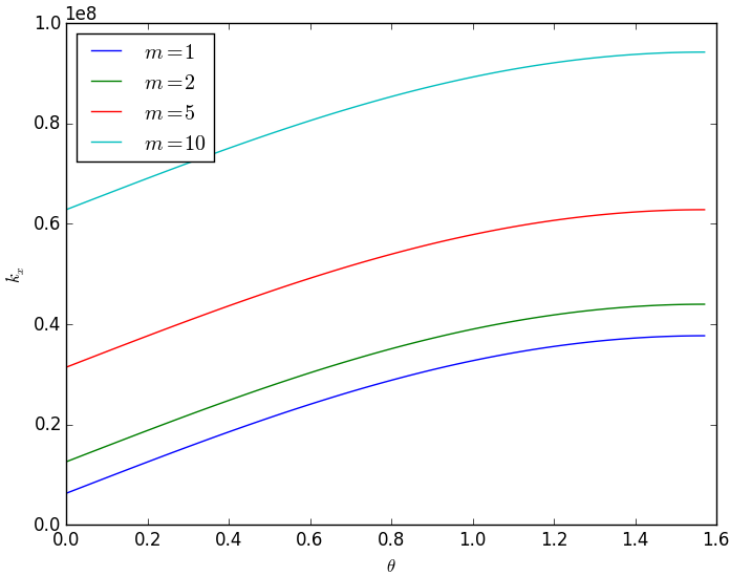

Figure 3.5: Phase addition from a single diffraction mode, m, from the grating.

surface is rough and has any form of periodic perturbations, then the light will also be diffracted off of the surface at angles other than the angle of reflection. These diffracted modes are denoted as stated above and if a diffracted mode has propagation constant k_m, that is greater than k_L, it will not propagate in free space but will become an evanescent wave. Figure 3.5 uses Eqn. (35) to show the propagation constant of the light produced along the interface versus the incident angle of the light beam.

$\lambda_L = 200$ nm and $a = 1$ μm. From Figure 3.2, a particle velocity of $v_p = \frac{c}{10{,}000}$ intersects the SPP dispersion curve at a wave number of $k \sim 2.2x10^{11}$. This means that the incident laser light needs to match this wave number. Figure 3.5 shows that the phase addition from a single diffraction mode of the grating is approximately $5x10^7$, therefore thousands of modes would need to have a propagation constant larger than k_L which is far from feasible because the intensity of the diffracted modes decrease as $\sim \frac{\sin^2 x}{x^2}$ [50]. Only a handful of diffraction modes will be strong enough to contribute to the increase in the propagation constant of the incident light.

Making a 2D array of nanoholes makes little change to the situation. The phase matching condition needs to be changed to account for any rotation that may occur between the plane of incidence of the light and the wave vector of the grating. Eqn. (35) now becomes [51]. Since the end-goal of this SPP excitation is to accelerate ions thru the holes in the nanohole array, the holes cannot be completely filled with a non-air dielectric as eluded to when the surface plasmon limiting value was determined above. This implies that a sleeve of optically transparent material with a permittivity greater than air should be used inside the holes. If a gap is also fabricated between the dielectric sleeve and the

metal sides of the cylinder, prism coupling in the Otto configuration [43] can be harnessed to achieve some wave propagation modification in addition to the grating coupling.

$$k_{sp}{}^2 = \epsilon_0 k_L{}^2 \sin^2\theta + \left(\frac{2m\pi}{a}\right)^2 \pm 2\sqrt{\epsilon_0} m \frac{2\pi}{a} k_L \sin\theta \cos\varphi. \quad (36)$$

Propagation constant alteration occurs when light traveling through a dielectric undergoes total internal reflection (TIR) and creates an evanescent field at the location of TIR. The in-plane momentum in the evanescent field is defined by

$$k_x = k_L \sqrt{\epsilon_0} \sin\theta. \quad (37)$$

An inhibitor to the Otto configuration scheme is that it can only excite SPP's at the metal/air interface with wave vectors in the region between the air light line and the prism light line. The maximum increase in k is defined as $k = k_0 n$ where n is the index of refraction of the dielectric. Combining these two schemes produces an increase in k of

$$k_x = \sqrt{\epsilon_0} k_L \sin\theta \pm \frac{2m\pi}{a} + k_L \sqrt{\epsilon_0} \sin\theta = 2n_0 k_L \sin\theta + \frac{2m\pi}{a} = 1.88\text{x}10^8 \text{m}^{-1}. \quad (38)$$

with a maximum obtained for $\theta = \pi/2, m \cong 7$ and $a = 500$ nm. The slowest particles that can be interacted with by SPP's in this geometry have velocities $v_p \cong c/5$.

For the particles to be accelerated by the SPP's, there needs to be a transfer of energy between the excited SPP's and the traveling particles. Further study of Figure 3.2

shows that the SPP's become surface plasmons in the limit of large k/k_p, approximately $v_p \cong c/1000$. This means that the dispersion curve plateaus and therefore the group velocity defined by $d\omega/dk$ goes to zero. The group velocity of a wave is defined when the wave is considered dispersive, such that its velocity depends on ω and/or k. Each constituent sinusoidal wave that makes up a resultant wave packet propagates with a different phase velocity (Figure 3.6).

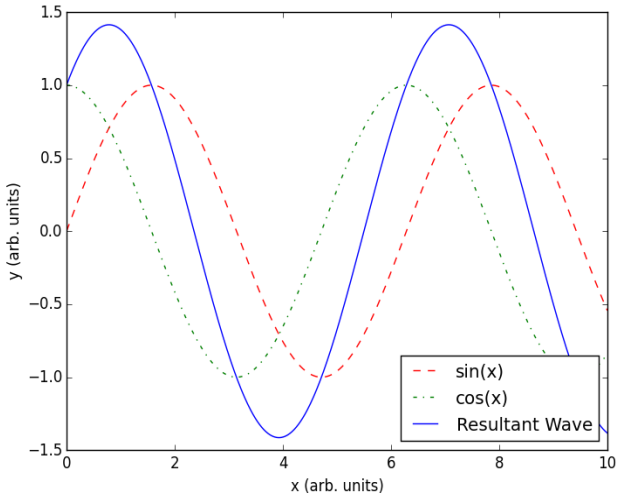

Figure 3.6: Individual sinusoidal waves and their summed resultant wave packet.

The velocity that defines the propagation of the resultant wave packet is the group velocity and it is this velocity that is the so-called measured velocity [52]. The kinetic energy of the wave is determined by this measured velocity, or the group velocity. Energy is propagated in a wave by the group motion of any superimposed phases. Therefore, even if a method can be contrived for SPP's to interact with particles of a slow velocity, such as $c/1000$, the SPP's will be in their limiting state of the surface plasmon and will be unable to transfer energy to accelerate the particles.

4. DIELECTROPHORETIC PROPELLANT INJECTION

The manipulation of micro/nanoparticles of solid or aqueous material by way of gradient electromagnetic fields is used extensively in the fields of photonics and microfluidics. One such action mechanism is that of the dielectrophoretic force. Dielectrophoresis is well known and has been utilized in the manipulation of liquid microflows and pico/nanoliter droplets for siphoning[53], separation and mixing[54] in chemical and biological experiments, and transport applications[55]. Liquid tendrils have been guided from a droplet along wall-less straight[56] and curved[57] virtual microchannels by way of the dielectrophoretic force enabling enhanced flexibility for the aforementioned transport techniques. Additional nanoparticle manipulation schemes make use of plasmon generated gradient force fields which have been studied for the acceleration of net-neutral nanoparticles via dielectrophoresis with applications in nanosatellite propulsion systems[19-21]. In this section, a dielectrophoretic tilted plate geometry is studied that enables variable injection of nanoparticles or microliter quantities of liquids into manipulation/acceleration schemes such as those mentioned above and can double as a mass storage reservoir when injection is inactive.

4.1. DIELECTROPHORESIS BACKGROUND

Dielectrophoresis occurs when a net-neutral particle is placed in a non-uniform electric field. The electric field polarizes the particle and the polarized particle then feels a force due to the gradient in the magnitude of the field (Figure 4.1). The direction of the force depends on the difference between the permittivity of the particle and that of the

surrounding medium. The dielectrophoretic (DEP) force is utilized in a variety of research fields but most commonly in microfluidics and biomedical applications [58]. Its effectiveness in these areas is due, in part, to its ability to separate particles according to their polarizability and/or size. We desire to make use of its ability to precisely control the motion/flow of a concentration of net-neutral nanoparticles.

Research has shown that dielectrophoresis can be used to continuously pump particle-laden microfluidic flows through virtual (wall-less) channels using microstructured electrodes in a variety of configurations [55]. Research has also shown that dielectrophoresis can filter particles from a stream of gas; expanding the usability of the DEP mechanism [59]. Further progress in this field has demonstrated that particulate matter can be separated by use of dielectrophoresis in a vacuum environment, known as vacuum dielectrophoresis [60]. Vacuum dielectrophoresis eliminates certain interactions due to the particles moving in a medium/fluid, making the DEP force the only interaction with the particles in the plane perpendicular to the force of gravity.

In Figure 4.1, a comparison is made of the motion of particles placed in a uniform electric field (a) versus those placed in a non-uniform field (b). Figure 4.1 (a) depicts a negatively charged particle (an electron) and a net-neutral particle in the presence of a uniform electric field. The electron is attracted by the anode and repelled by the cathode via the Coulomb force. Whereas the neutral particle feels a force by both electrodes that is equal in magnitude yet opposite in direction such that the particle feels no net force. The non-uniform field in Figure 4.1 (b) indicates the motion of two net-neutral particles of differing material composition. If an electron were placed in this field it would behave as expected and travel towards the anode. The electric field polarizes the net-neutral

particles and, due to the non-uniformity of the field across the particles, a net force is produced that causes each particle to move towards or away from the region of greater field strength. Positive (Negative) dielectrophoresis, pDEP (nDEP), describes the case in which the particle moves up (down) the gradient of the magnitude of the electric field. Net-neutral nanoparticles, the propellant of our plasmonic thruster system, are injected into the plasmonic accelerator structure by the DEP force which arises from the non-uniformity of the electric field.

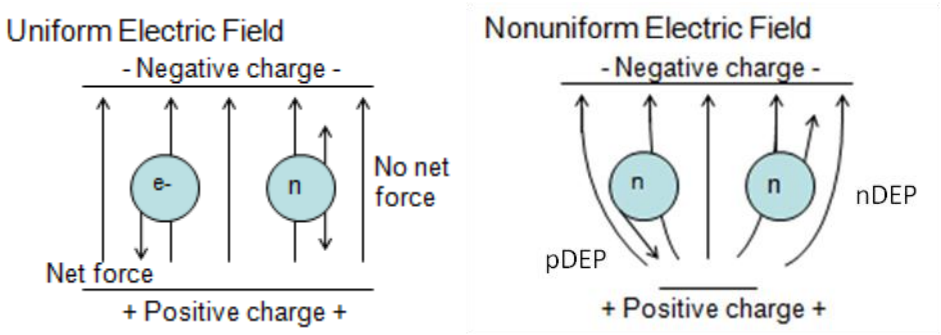

Figure 4.1: Particle motion in uniform vs non-uniform electric fields.

The DEP-induced motion depends on the dielectric properties of the particles and the surrounding medium. Specifically, it depends on the effective polarization of the suspended particles. If the polarizability of a net-neutral nanoparticle is greater than the polarizability of the surrounding medium, then the nanoparticle will be pushed toward the stronger region of the electric field (pDEP) and vice-versa (nDEP) if the medium has higher polarizability. Eqns. (39) and (40) define the DEP force acting on a particle. R is the radius of the particle. ε_m is the permittivity of the surrounding medium in which the particles are suspended. k is the Clausius-Mossotti factor, defined in Eqn. (40), that

$$\vec{F}_{DEP} = 2\pi R^3 \varepsilon_m k \nabla\left(\left|\vec{E}\right|\right)^2. \tag{39}$$

$$k = \frac{\epsilon_p - \epsilon_m}{\epsilon_p + 2\epsilon_m}. \tag{40}$$

relates the permittivity of the particle and medium and is positive when the particle permittivity is greater than the medium permittivity. $\vec{E}$ is the electric field. From these equations we see that the DEP force is proportional to the cube of the radius of the suspended particles as well as the gradient of the magnitude of the electric field.

4.2. DEP PROPELLANT INJECTOR

The DEP force can be used to inject nanoparticles into a photonic particle manipulator. As described above, the DEP force is active in the presence of a non-uniform electric field. It acts on net-neutral particles along the direction of the gradient of the non-uniform field. Therefore, to harness the DEP force and use it to propel nanoparticles into particle manipulating platforms, we must design an electric field that is non-uniform and whose gradient tends to lie along a single direction. We investigate here a wedge-shaped prism, whose 2-D cross section is a simple tilted plate capacitor. This geometry creates a steady, non-uniform electric field supplied by a DC voltage and the electric field can be easily solved analytically in 2-dimensions using the following equation derived from Coulomb's Law for the electric field due to a distributed charge.

For 2-dimensions, let the charge density $\rho(\vec{r}') \rightarrow \lambda(\vec{r}') = Q/L$ where Q is the charge on the plate and L is its length. With this reduction and the definitions in Eqns. (42), (43) and (44) that give the location of a test point and shape of the surfaces, we can

$$\vec{E}(\vec{r}) = \frac{1}{4\pi\varepsilon_0}\int \rho(\vec{r}')\frac{\vec{r}-\vec{r}'}{|\vec{r}-\vec{r}'|^3}\,d^3\vec{r}'. \tag{41}$$

define the total electric field between the surfaces as the sum of the electric fields produced by each plate, Eqn. (45). Figure 4.2 illustrates the variables in Eqns. (42)-(44).

$$\vec{r} = y_0\hat{j} + z_0\hat{k}. \tag{42}$$

$$\vec{r}_L{}' = y'\hat{j} + (my' - h)\hat{k}. \tag{43}$$

$$\vec{r}_U{}' = y'\hat{j} + (h - my')\hat{k}. \tag{44}$$

$$\vec{E}(\vec{r}) = \overrightarrow{E_U}\big(\vec{r}(y,z)\big) + \overrightarrow{E_L}\big(\vec{r}(y,z)\big). \tag{45}$$

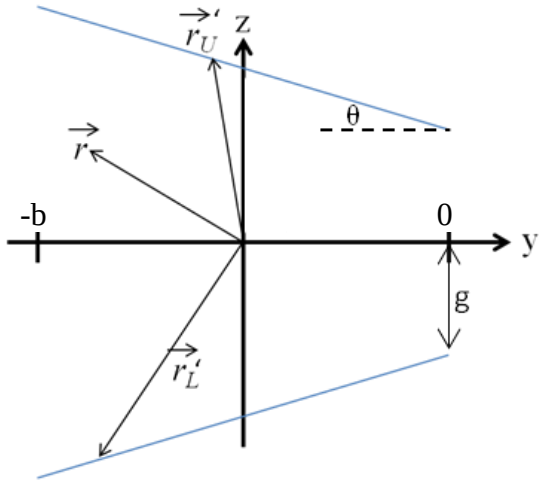

Figure 4.2: Visual definitions of variables in Eqns. (42), (43) and (44). $b = 50\ \mu m, g = 7\ \mu m, \theta =$ variable.

The tilted plate capacitor cross-section is shown in Figure 4.3, where the red lines show the silhouette of the injector, and the design is such that the particles will start in the injector (injector doubles as a storage tank) and then exit to the manipulation platform on the right. The upper and lower surfaces of the injector (red lines in the image) are electrically separated and a potential difference is maintained across them in order to produce the desired electric field. A dielectric, rectangular guide-sleeve (solid blue lines) is inserted along the axis of the injector between the charged surfaces with separation distance equal to the opening width, 2g, of the injector exit. The dielectric guide sleeve keeps the particles away from the plates where, in close proximity to the plates, the gradient of the electric field pointing toward the plate acts to trap them in pDEP.

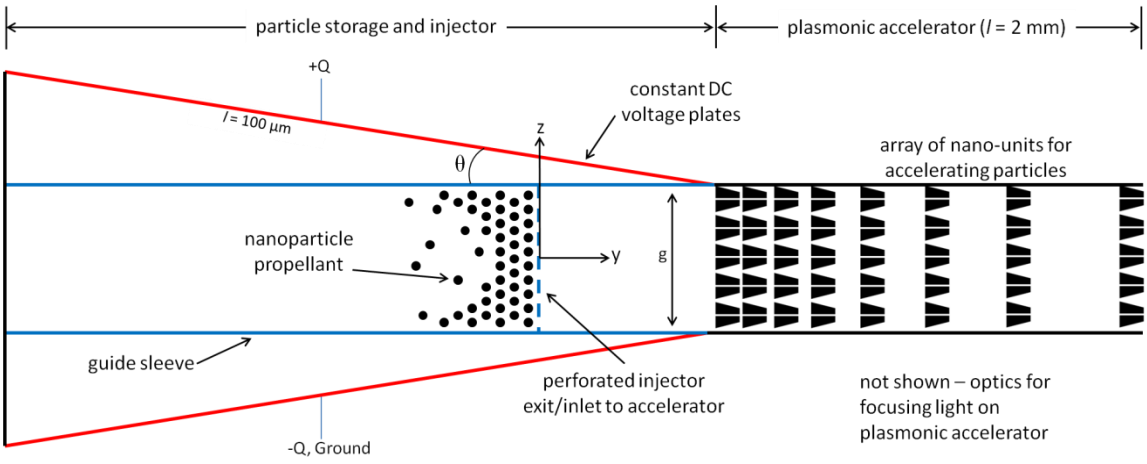

Figure 4.3: Geometry of trapezoidal prism propellant injector.

Summing the electric fields due to both plates allows the conversion of Eqn. (41) to Eqn. (45) with $\overrightarrow{E_L}$, the electric field produced by the lower plate, defined by Eqn. (46) and $\overrightarrow{E_U}$, the electric field produced by the upper plate, defined in Eqn. (47).

$$\overrightarrow{E_L}\left(\vec{r}(y,z)\right) = \frac{Q}{4\pi b\varepsilon_0}\int_{-b}^{0}\frac{(y_0-y')\hat{j}+(z_0-my'+h)\hat{k}}{((y_0-y')^2+(z_0-my'+h)^2)^{3/2}}dy'. \quad (46)$$

$$\overrightarrow{E_U}\left(\vec{r}(y,z)\right) = \frac{-Q}{4\pi b\varepsilon_0}\int_{-b}^{0}\frac{(y_0-y')\hat{j}+(z_0+my'-h)\hat{k}}{((y_0-y')^2+(z_0+my'-h)^2)^{3/2}}dy'. \quad (47)$$

The electric field produced by this setup is plotted in Figure 4.4 (a) for plate angle $\theta = 0.0°$ and Figure 4.4 (b) for $\theta = 25°$. For validation, the $\theta = 0°$ case is compared to the electric field produced by a parallel plate capacitor, which assumes infinite electrodes, $E_{cap} = V/d$. E is the electric field, V the electric potential difference between the two electrodes, and d the separation distance between the two capacitor electrodes. With $V = 2.0\ V$ and $d = 14\ \mu m$, $E_{cap} \cong 142.9\ kV/m$. Let $V = 2.0\ V$ and $d = 14 \pm 0.16\ \mu m$ for the analytical model solution with finite electrodes. The minor difference in plate separation values is an intentional offset for the analytical solution because the electric field derived from Coulomb's law is proportional to $1/r^2$, which means that as d approaches $14\ \mu m$, the distance to the second plate approaches zero and the electric field contribution goes to infinity. The electric field produced by the plates in the analytical solution, at the point $y = -25\ \mu m, z \cong 7\ \mu m$ where the field is max, is $E_{analytical} \cong 143.5\ kV/m$. The percent error between the finite plate analytical and infinite plate parallel capacitor solutions is $0.42\ \%$ .The electric field distribution in Figure 4.4 (b) for the $\theta = 25°$ plate angle is steady and non-uniform, increasing in strength from left to right. The solid, black, diagonal lines represent the edges, or silhouette, of the wedge-shaped injector while the short vector lines indicate the electric field produced between the electrodes. Along the centerline ($z = 0$), one can see that the electric field lines

increase in strength with increasing y-position. These properties are plotted in Figure 4.5. We have disregarded the configuration of the electric field outside of the particle injection structure because it has no effect on the motion of the particles and is assumed to be shielded.

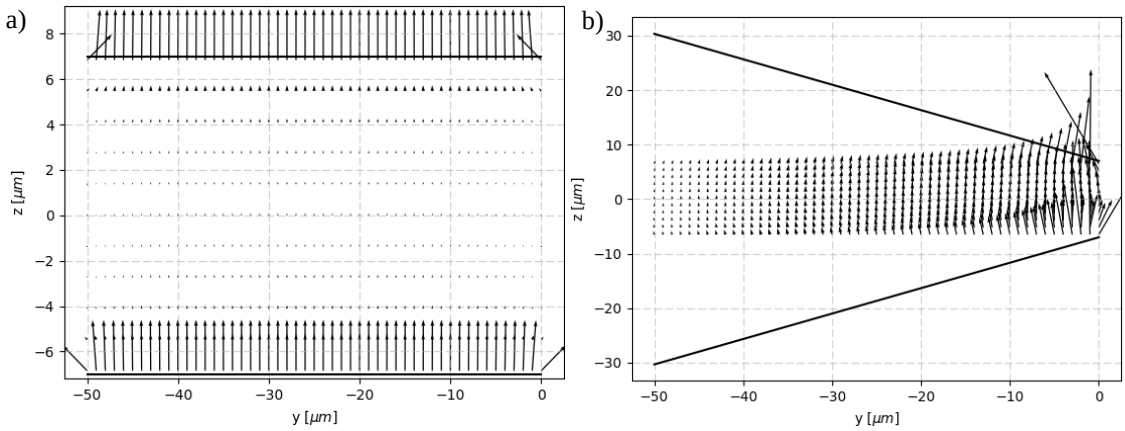

Figure 4.4: Electric field vectors between electrodes with plate angle (a) $\theta = 0°$ and (b) $\theta = 25°$.

In Figure 4.5, contours of the electric field along the centerline and 3 μm above and below the centerline are plotted versus the distance along the axis of the injector. E_z and E_y are the electric field components in the z- and y-directions, respectively. The dotted red line in Figure 4.5 shows that the y-component of the electric field along the axis of the injector is zero for the whole axis. This is expected because as the electric field lines curve from one electrode to the other, they are perpendicular to the centerline axis of the injector at the centerline. The off-axis y-components of the electric field contour show that there is a transition region where the electric field reverses direction inside the injector (yellow dotted line and black dot-dash line at $y \approx -4.5$ μm). This

phenomenon poses a potential problem because the gradient of the electric field also changes sign (observe the slope of the yellow dotted line and black dot-dashed line for $-15\ \mu\text{m} < y < -5\ \mu m$) which could indicate a trapping region for the nanoparticles if pDEP is utilized. The transition region is also visible in the slope of the off-axis contours of the z-component of the electric field (blue solid, red dot-dot, and cyan dash lines for $-7.5\ \mu\text{m} < y < -2.5\ \mu m$).

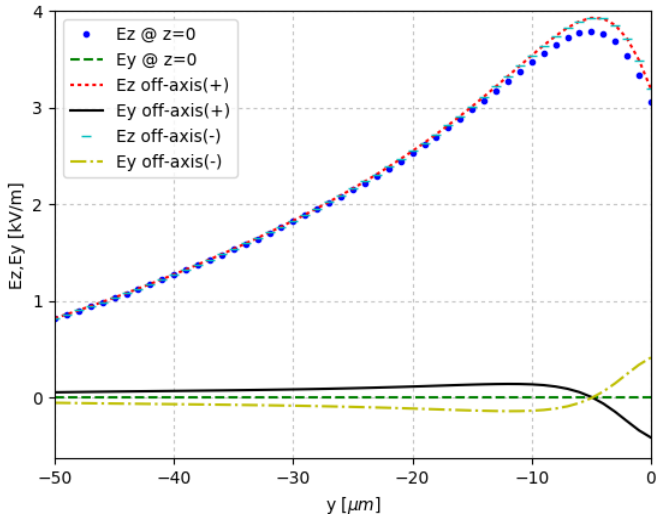

Figure 4.5: Axial and transverse electric field line contours between angled electrodes.

As stated previously, the DEP force is calculated from the gradient of the magnitude of the electric field. Figure 4.6 contains contour plots of the gradient in the (a) y-direction and (b) z-direction (the signed natural logarithm is used to create a higher contrast visual of the data) and Figure 4.6(c) is a line contour of the characteristic force along the axis of the injector. The characteristic force is the DEP force divided by the cubed radius of the nanoparticles such that Eqn. (39) becomes Eqn. (48) with units of N/m^3. ε_m, the dielectric permittivity of the surrounding medium, is set to

$8.854\text{x}10^{-12}\,\frac{s^4A^2}{m^3kg}$, the permittivity of free space. ϵ_p, the dielectric permittivity of the particles, $23\text{x}10^{-12}\,\frac{s^4A^2}{m^3kg}$.

$$\frac{\vec{F}_{DEP}}{R^3} = 2\pi\varepsilon_m k\nabla\left(\left|\vec{E}\right|\right)^2. \tag{48}$$

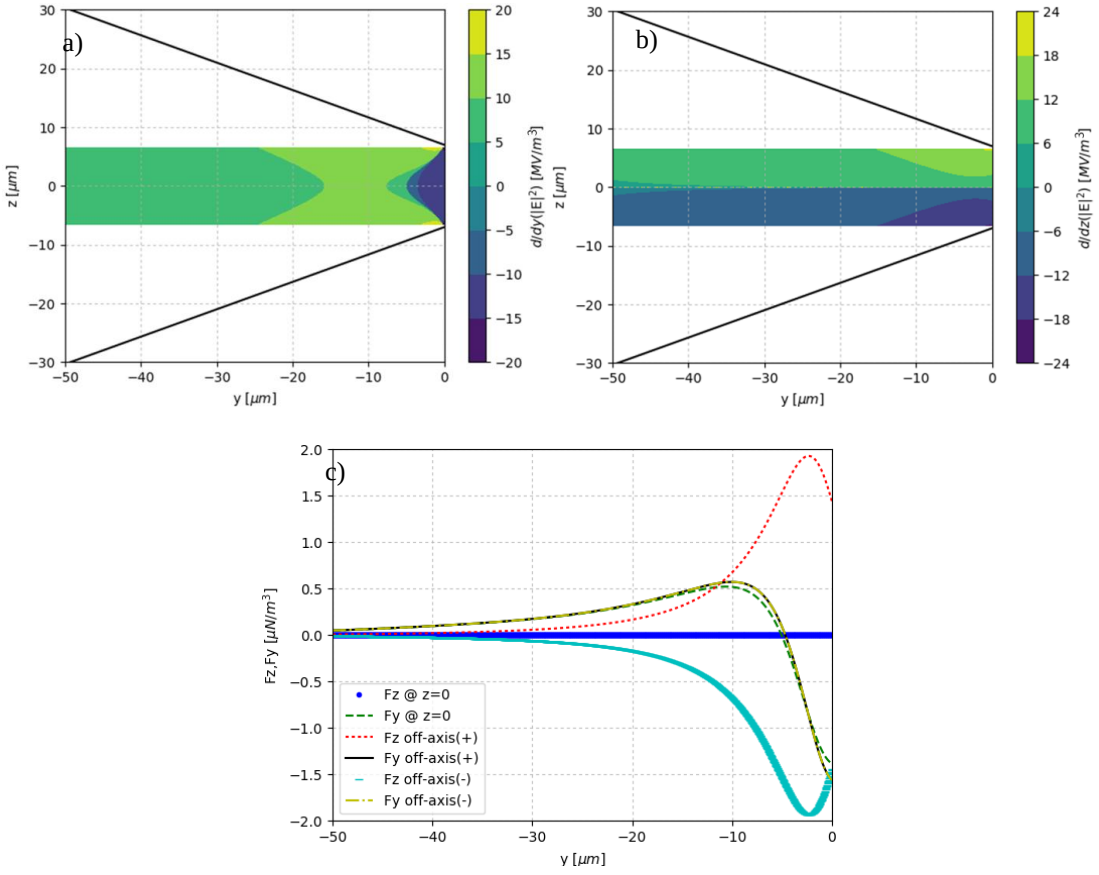

Figure 4.6: Injector electric field profiles (a) Y-Gradient of the magnitude of the electric field, (b) z-gradient of the magnitude of the electric field, (c) dep force profile along axis of angled electrodes (at the centerline and ± 3 μm off the centerline) (plate angle 25°).

The force in the y- and z-directions at three values of $z = 0, 3, -3$ μm are plotted in Figure 4.6 (c). F_y for all three z values begins positive and then goes negative near

$y \cong -5\ \mu m$. Studying the y-gradient of the electric field magnitude indicates that this behavior is expected because following the gradient from left to right in Figure 4.6 (a), along the axis, one sees that the gradient begins positive, increases, then decreases and goes negative. The force is proportional to this profile as shown in Eqn. (48). Contrary to F_y, F_z behaves differently for each z value. When $z = 0\ \mu m$ the force in the z-direction is also zero along the entire axis because the z-gradient of the electric field magnitude crosses an inflection point in this location. When $z = 3\ \mu m$ the z-gradient is positive which shows the electric field increasing toward the electrode as the $1/r^2$ dependence indicates it should. Increasing y position effectively brings the electrode closer to the $z = 3\ \mu m$ line which also follows the $1/r^2$ dependence and we see a corresponding increase in F_z. When $z = -3\ \mu m$, F_z mirrors the behavior of F_z when $z = 3\ \mu m$. The force is negative, pointing along the gradient directed towards the lower electrode.

4.2.1. Parametric Analysis. A parametric analysis was performed to develop a more comprehensive understanding of the dependence that the DEP force has on the plate angle, θ, of the charged plates as well as their separation distance, g. In Figure 4.7 (a) the largest force magnitude produced in the y-direction (positive or negative) within the guide sleeve is plotted for three electrode plate separation distances and various plate angles. This value is determined for each plate angle by calculating the maximum of the absolute value of the force in the y-direction then re-introducing the sign of the force value so as not to lose information regarding which direction the maximum force acts. Figure 4.7 (b) indicates the average force in the y-direction, calculated as the statistical mean of F_y within the entirety of the guide sleeve area, and (c) shows the associated standard deviation from that statistical average.

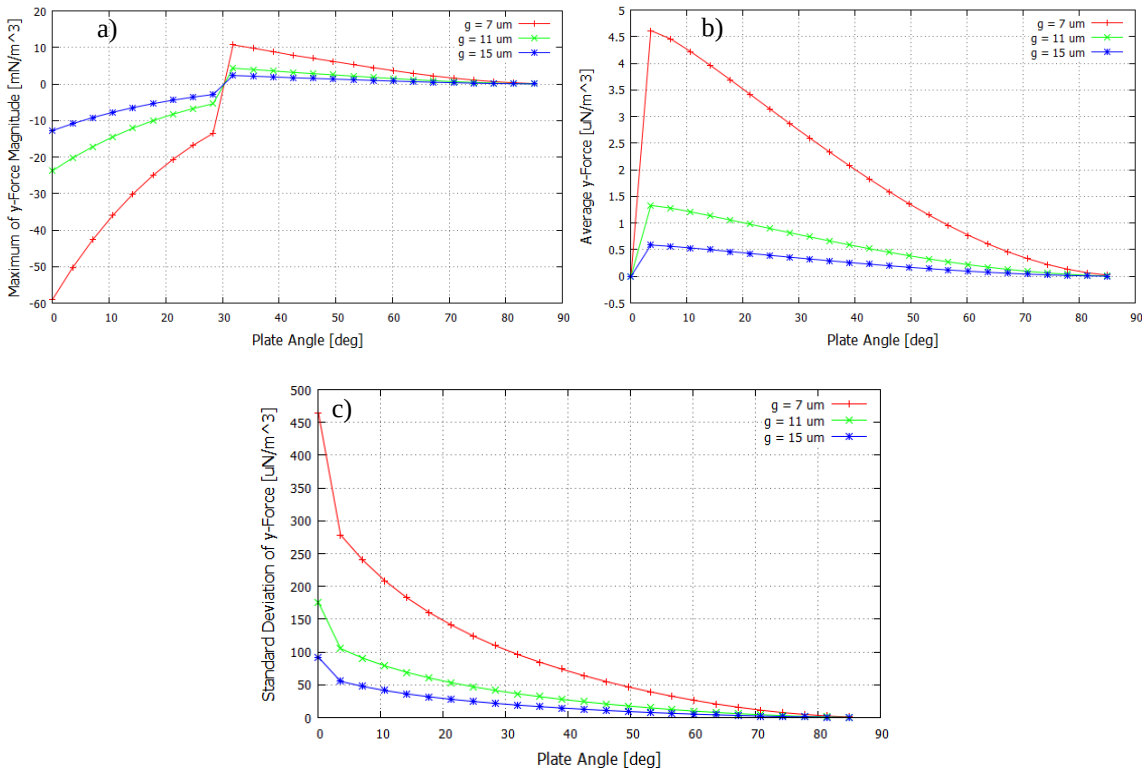

Figure 4.7: Force results from injector parametric analysis (a) Maximum force magnitude in the y-direction, (b) average force in the y-direction, (c) standard deviation of the force in the y-direction; (a), (b), and (c) each vs. plate angle and separation distance of the guide sleeve within the gap of the DEP injector.

Addressing the separation distance, g, the maximum y-force magnitude plotted in Figure 4.7 (a) increases as g decreases. The discontinuity at 30° occurs when the positive values of the gradient of the electric field become stronger in magnitude than the negative gradient values, as explained later in this section. From Figure 4.6 (a), we expect the magnitude of the force to be greatest where the electric field gradient is strongest, such as in the region that y is between -5 µm and 0 µm. In this region the gradient is negative meaning the force will also point along the negative y-direction as seen in Figure 4.7 (a) for plate angles less than 30°. For plate angles greater than 30° Figure 4.7 (a) indicates that the max force is positive in the y-direction. This can be explained by analyzing the

field region of the example contour plot shown in Figure 4.8 (a), for plate angle 35°, near the electrode and at the narrow end of the particle injector where an increase in the strength of the positive gradient of the field occurs (annotated in Figure 4.8 (a)).

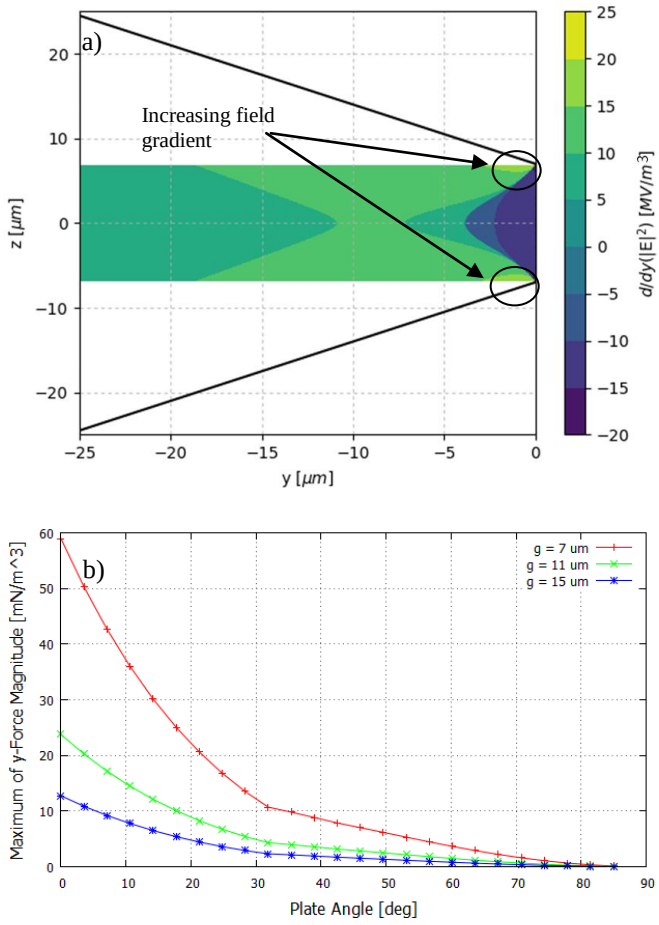

Figure 4.8: Field region analysis of injector (a) Y-Gradient of the magnitude of the electric field (plate angle 35°), (b) maximum force magnitude in the y-direction.

The positive gradient values in the Figure 4.8 (a) contour increase by $\sim 5\ \mathrm{MV/m^3}$ when compared to the positive gradient values in the plot in Figure 4.6 (a). (The light green contour represents values 15-20 $\mathrm{MV/m^3}$ and the yellow contour 20-25 $\mathrm{MV/m^3}$ versus the previous plot of light green 10-15 $\mathrm{MV/m^3}$ and yellow 15-20 $\mathrm{MV/m^3}$). This

makes the largest positive gradient greater than the smallest negative one such that the maximum force magnitude in the y-direction for plate angles greater than $30°$ is positive. The piece-wise step from negative to positive max force values, though interesting, is not the important information from Figure 4.7 (a). Converting the data from Figure 4.7 (a) into the simple, unsigned magnitude of the maximum y-force versus plate angle and plotting it in Figure 4.8 (b) indicates that, as the plate angle increases, the gradient, and thus the force in the y-direction, decreases in strength. The above analysis of the maximum y-force magnitude indicates that small plate angle and narrow plate separation distance are preferable in order to generate strong DEP force fields.

Analysis of the average y-force plotted in Figure 4.7 (b) indicates the same conclusion. As the plate angle increases, the regions where the electric field gradient is strongest decrease in size which can be seen by comparing Figure 4.6 (a) to Figure 4.8 (a). The strong positive gradient region between $y = -25$ μm and -2 μm in Figure 4.6 (a) decreases in size to a region between $y = -18$ μm and -2 μm in Figure 4.8 (a) while simultaneously maintaining strength at $\sim 10\ \mathrm{MV/m^3}$. This decrease in region size of the strong gradient brings down the overall average of the electric field gradient and subsequently the force. We expect the average y-force to be zero, as seen in Figure 4.7 (b), when the plate angle is zero because any fringe effects at the ends of the charged plates will be equal and opposite when the injector structure is mirrored across the vertical line $y = -25$ μm. The $\theta = 0°$ structure plotted in Figure 4.4 (a) exemplifies these mirrored fringe effects where it can be seen that the electric field points outward at both ends of the bottom plate and inward at both ends of the upper plate. Analysis of the y-force deviation from the statistical average plotted in Figure 4.7 (b) indicates that

choosing a larger plate separation distance and larger plate angle produces a more consistent force field in the y-direction, yet, an overall weaker force.

The analytical solution is used to study particle dynamics within the tilted plate injector. COMSOL Multiphysics numerical models were also developed in order to study more complex electrode geometries and electric field structures. The initial geometry used for the numerical models is composed of the tilted, charged plates and the dielectric guide sleeve that restricts the motion of the nanoparticles. Figure 4.9 shows a contour plot of the magnitude of the electric field between the two tilted plates. The field structure supports our understanding of the analytically obtained results in Figure 4.4 (b) wherein the field strength increases towards the narrow end of the injector and near the electrodes. The electric field magnitude at location

The perforated exit/inlet membrane that guides the injection of the nanoparticles, indicated in Figure 4.10, was also included in COMSOL models to determine its affect on the electric field structure. Our design calls for a metallic membrane that acts as a floating

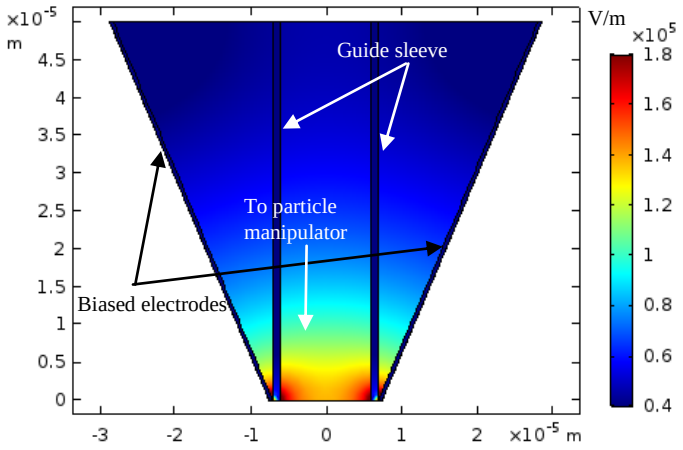

Figure 4.9: COMSOL Multiphysics model of electric field magnitude in tilted plate injector (injector in this image is rotated 90° clockwise and is pictured with the hollow dielectric guide sleeve).

potential and shields part of the dielectric guide sleeve from the applied electric field at the location where the electric field gradient changes direction as indicated in Figure 4.5. A concern we have with this membrane is that the electric field will reduce to zero too quickly at the location of the perforations and the resultant gradient will create a strong DEP force acting against the motion of the nanoparticles. Figure 4.10 shows the force field contours for the tilted plate injector with a perforated metallic membrane acting as a floating electrical ground. The perforations in the membrane are perpendicular to the axis of the injector and act as a gate through which the nanoparticles pass. From this contour plot, we see that the presence of the metallic membrane does create force acting against the motion of the particles (the red/orange/yellow bulge in the center of the plot, focused at the perforated membrane).

The DEP force depends on the relative polarizability of the nanoparticles to the surrounding medium which is vacuum, as stated earlier. This means that the dielectric constant of the nanoparticles is greater than the dielectric constant of the medium, vacuum, and the DEP force takes on the sign of the gradient of the electric field

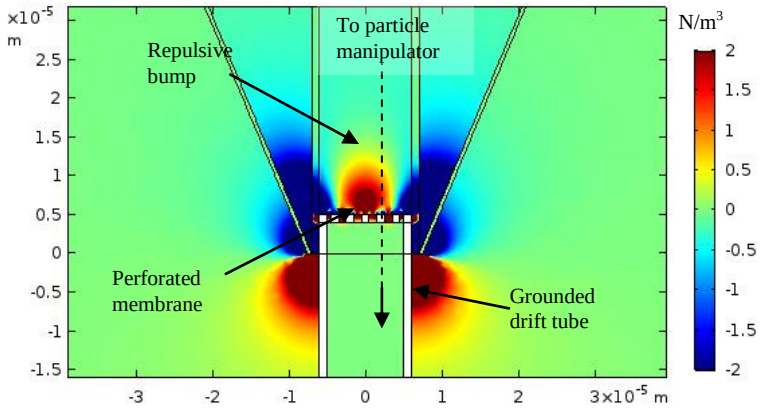

Figure 4.10: COMSOL Multiphysics model of force field in tilted plate injector with dielectric guide sleeve and metallic perforated membrane as floating ground.

magnitude. If the medium had a dielectric constant that was greater than that of the nanoparticles then the DEP force would be the negative of the sign of the gradient in the electric field magnitude. Therefore a possible solution to the strong negating force issue that the perforated membrane poses is to suspend the nanoparticles in a liquid such as water ($\varepsilon_m = 710\text{x}10^{-12}\,\frac{s^4A^2}{m^3kg}$) rather than vacuum ($\varepsilon_m = 8.854\text{x}10^{-12}\,\frac{s^4A^2}{m^3kg}$). The resulting force field contour of the tilted plate injector that is filled with water and has a dielectric guide sleeve and a metallic perforated membrane is plotted in Figure 4.11. This contour shows that the repulsive hump seen in Figure 4.10 now becomes an accelerating ramp that assists the motion of the nanoparticles.

4.2.2. Particle Dynamics. The injection rate, in particles per second, needs to be calculated in order to determine the thrust profile of the system. The particles upstream cause a pressure buildup on the particles near the interface with the thruster such that the exiting particles are pushed into the thruster. This means that the pressure force will decrease over time as the total number of particles in the tank decreases, therefore the particle injection rate will change and subsequently the thrust. In the following sections

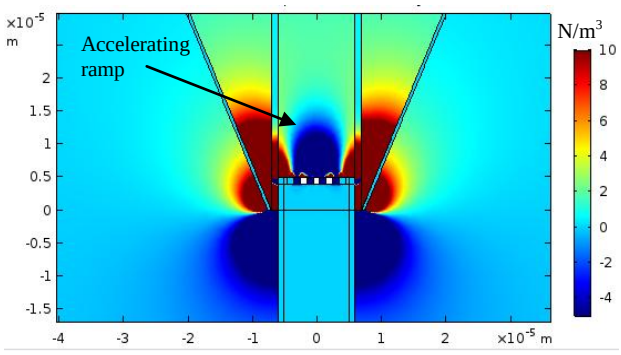

Figure 4.11: COMSOL Multiphysics model of force field in tilted plate injector with water as the suspension material, a dielectric guide sleeve, and a metallic perforated membrane as floating ground.

we consider the motion of the propellant inside the injector and to the thruster. The propellant consists of nanoparticles whose motion can be analyzed by using a particle dynamics simulation.

The motion of each particle is Newtonian in nature and defined in Eqn. (49).

$$F_{np} = mg + f_{wall} + f_{pars} + f_{DEP} \tag{49}$$

F_{np} is the force acting on a nanoparticle. mg is the gravitational force and is neglected while the smallsat is in orbit which coincides with operation of the DEP injector. f_{wall} is the force acting on a particle during a particle-wall collision. This force is zero unless a particle collides with a wall. Likewise, f_{pars} is the force acting on a particle during a particle-particle collision and is zero unless this type of collision occurs. f_{DEP} is the dielectrophoretic force defined in Eqn. (39) and is zero unless the DEP injector is turned on. For simplicity and to reduce computation time, all simulations are performed on a 2-dimensional slice of the injector-thruster geometry, Figure 4.3. All collisions are approximated as elastic with coefficients of restitution CORw = 0.7 and CORp = 0.65 for particle-wall and particle-particle collisions, respectively.[61,62] The coefficient of restitution approximates the kinetic energy removed from a moving propellant particle during a collision. CORw = 0.7 is chosen as the average coefficient of restitution of glass and quartz, as measured by Whitaker, et. al. [62], to represent an arbitrary dielectric material that composes the guide tube. CORp = 0.65 is the measured coefficient of restitution for polystyrene determined by Constantinides, et. al. [61] When a particle-particle collision occurs, the pre-collision state vectors of each particle combined with the

conservation of momentum and energy are used to define the post-collision state vectors such that the post-collision velocities are defined in Eqns. (50)-(53). The subscripts 1 and 2 differentiate the particles involved in the collision. u indicates the pre-collision velocities of each particle whereas v indicates the post-collision velocities. θ defines the angle between a reference coordinate frame and a body-centered coordinate frame for which the x-axis is collinear with the center of mass of both colliding particles.

$$v_{1,x} = \mathrm{CORp}\left(u_{2,x}\cos^2\theta + u_{1,x}\sin^2\theta + \sin\theta\cos\theta\left(u_{1,y} - u_{2,y}\right)\right). \tag{50}$$

$$v_{1,y} = \mathrm{CORp}\left(u_{1,y}\cos^2\theta + u_{2,y}\sin^2\theta + \sin\theta\cos\theta\left(u_{1,x} - u_{2,x}\right)\right). \tag{51}$$

$$v_{2,x} = \mathrm{CORp}\left(u_{1,x}\cos^2\theta + u_{2,x}\sin^2\theta + \sin\theta\cos\theta\left(u_{2,y} - u_{1,y}\right)\right). \tag{52}$$

$$v_{2,y} = \mathrm{CORp}\left(u_{2,y}\cos^2\theta + u_{1,y}\sin^2\theta + \sin\theta\cos\theta\left(u_{2,x} - u_{1,x}\right)\right). \tag{53}$$

A particle-wall collision is defined in much the same way except that the derivation is simplified greatly when considering a stationary wall. This allows for a

$$v_{y_f} = -\mathrm{CORw}\left(v_{y_i}\right),\ v_{x_f} = v_{x_i}. \tag{54}$$

basic recoil approximation where the particle velocity parallel to the wall is unchanged during the collision and the particle velocity perpendicular to the wall becomes negative

of what it was and is reduced by the coefficient of restitution. Eqn. (54) gives an example particle-wall collision for a wall perpendicular to the y-axis.

The particle locations and velocities are iteratively determined as time progresses in the simulation with time step equal to 100 ns as shown in Eqns. (55) - (58).

$$y_i = y_{i-1} + v_{y,i-1}t_{step} + \frac{1}{2}gt_{step}^2. \quad (55)$$

$$z_i = z_{i-1} + v_{z,i-1}t_{step}. \quad (56)$$

$$v_{y,i} = v_{y,i-1} + gt_{step}. \quad (57)$$

$$v_{z,i} = v_{z,i-1}t_{step}. \quad (58)$$

The step size is chosen small enough to prevent the occurrence of multiple particles occupying the same physical space after they move during an iteration. The nanoparticle propellant is considered to be settled when the mean velocity of all particles is less than 500 μm/s. This ensures that the location of each particle changes by less than $v_{par}t_{step} = 0.05$ nm on average between two time steps (this corresponds to a change in location of less than 0.1 % of the 50 nm radius of the nanoparticles). Simulating large systems of particles can be cumbersome and highly costly in terms of computation time. Therefore we track the motion of a small (Np ~ 10^2) number of particles, which greatly reduces computation time, and then extrapolate the characteristics to a larger system. Figure 4.12 shows an example particle distribution where the randomly distributed initial

positions are plotted in (a) and the final positions, after the particles have settled against the exit interface to the right of the plot, are in (b).

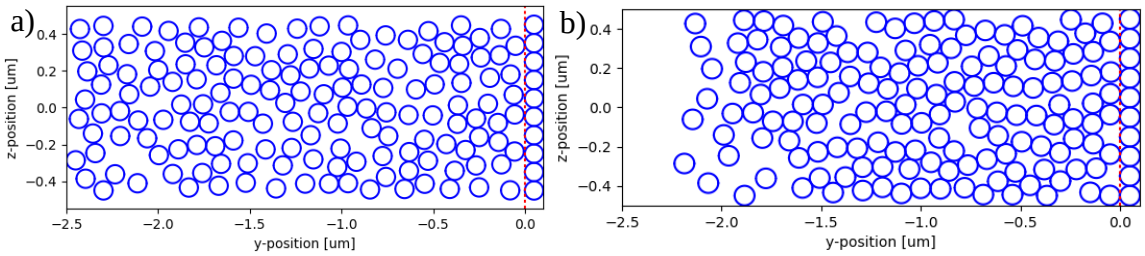

Figure 4.12: Particle propellant distribution (a) initial and (b) final positions of propellant particles for particle dynamics simulation.

Two test cases were run in which the relative radius of the particle to holes was varied and the number of particles emitted per iteration were determined which should reflect that variation. If the radius of the particles is greater than the radius of the exit holes then we expect no propellant to leave the injector. As expected, no particles exit the injector, Figure 4.13 (a). For the second test, we set the entire face of the exit plane as open, therefore if a particle would "strike" this plane it will exit the injector. As shown in Figure 4.13 (b), the maximum number of particles, five (based on the width of the exit and the size of the particles for this simulation), exit per time step for the entire operating time until the number of particles decreases. All further simulations are conducted with a hole radius set to five times that of the particle radius. (This value is determined by the critical radius which defines the ratio of hole radius to particle radius for which clogging does not occur due to arch structures developing in the granular material above a hole location. To prevent clogging the hole radius should be approximately 4.94 times that of an individual particle, for spherical particles. [63-65])

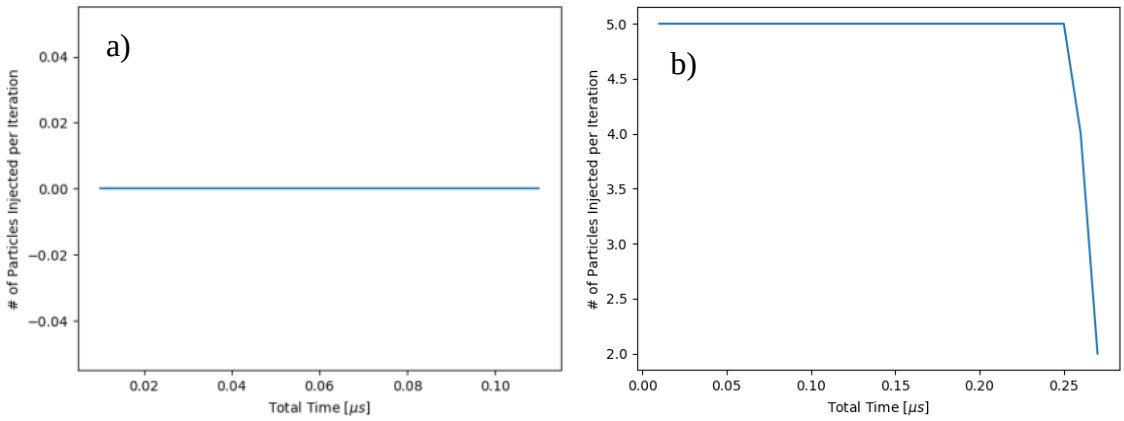

Figure 4.13: Number of particles exiting versus time. (a) radius of particles greater than radius of exit holes. (b) exit interface completely open.

When the propellant exits the injector, the velocity (specifically in the axial/y-direction) is recorded so that the thrust generated by the injector can be calculated. Once the propellant exits the injector it drifts for a short distance through a guide tube until it reaches the plasmonic thruster where it undergoes propulsive acceleration.

Figure 4.14 shows the average exit velocity that a particle has when it exits the injector and begins drifting toward the thruster versus the time step/iteration at which the

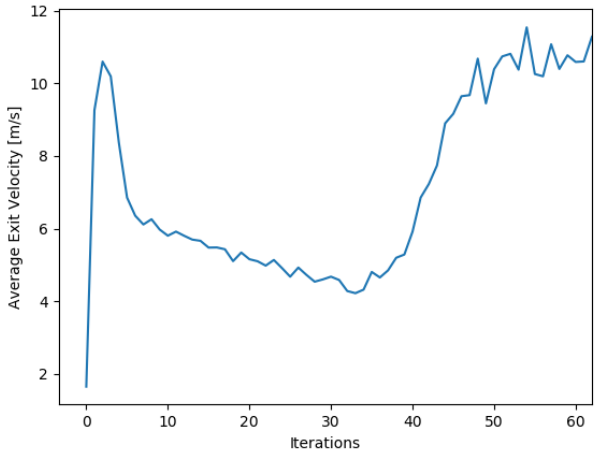

Figure 4.14: Average exit velocity in y-direction for each iteration in the simulation.

particle exited. We assume that the velocity perpendicular to the axis is negligible compared to the velocity in the direction of the axis.

Studying Figure 4.14 shows that the first particles to exit start from rest (a required condition), then after an initial spike in the exit velocity, there is a semi-steady state region between iteration 5 and 25 where the particles move, on average, in unison toward the exit plane. After this, at high iterations, we see that the exit velocity increases drastically. This is due to a decreased number of collisions in the propellant as the number of propellant particles has greatly diminished by this time as shown in Figure 4.15. With so few particles left in the injector, the remaining particles are able to build up high velocities before they interact with the exit plane and exit to the thruster or rebound.

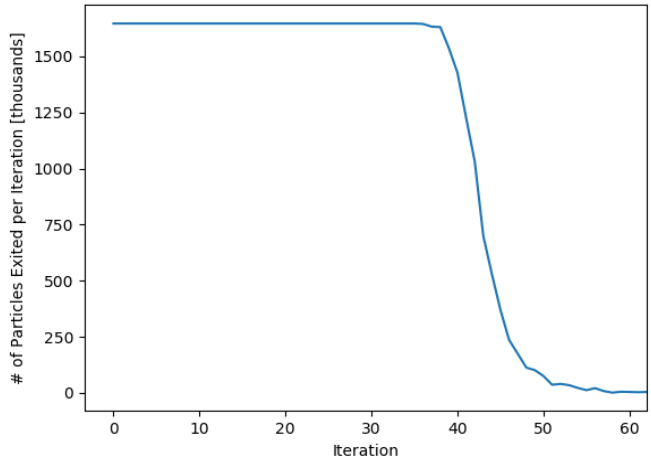

Figure 4.15: Number of propellant particles exiting the injector per iteration in simulation.

The system thrust is defined as the time-dependent thrust produced by the coupled dielectrophoretic injector and plasmonic thruster. We have found that simulating a system with few particles (to reduce computation time) leads to a fast depletion of the propellant

reserves. The thrust profile from the plasmonic thruster is calculated by iteratively determining the velocity for the propellant at each acceleration stage of the thruster as the propellant travels through the thruster. By iteratively determining the velocity of the propellant, we can calculate the thrust produced by each stage of the thruster assembly and record it as a function of time by multiplying the mass flow rate times the difference

Table 4.1: Particle system attributes to determine the generated thrust.

Simulated Particles:	72,050
Mass of Propellant:	2.8035e-18 kg
Shutter Speed of Pulsed Light:	10 μs
Length of Plasmonic Thruster:	2 mm

between the velocity of the propellant as it exits one nano-unit stage with the velocity it had when entering the stage. During this iterative process, we assume that the propellant

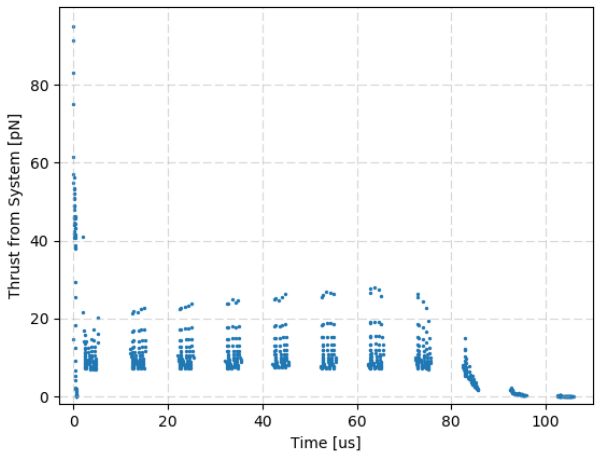

Figure 4.16: Thrust profile of the coupled injector-plasmonic thruster system.

is in-phase with the pulsed light source that dynamically excites the plasmonic thruster. This method produces an upper estimate of the thrust generated by the thruster because it does not account for propellant that may be out-of-phase with the pulsed light.

The thrust profile for an example system is given in Table 4.1 and Figure 4.16. We see the initial impulse from the injector that occurs between 0 and 0.5 μs followed by the short region of zero thrust that indicates the particles are drifting to the thruster. After this we observe the spikes in the thrust profile that define the propellant motion through the thruster.

5. CONCLUSIONS

The objective of this research focused on asymmetric nanostructures is to manufacture and investigate the characteristics and use of asymmetric, metallic, nanostructures for plasmonic force propulsion, a developing method of nano-/picosatellite thrust generation. Visible to near-infrared light is focused onto sub-wavelength nanostructures to generate polarized oscillations of electrons on the surface of the metallic nanostructures (surface plasmon polaritons). The surface plasmon polaritons accelerate nanoparticle propellant away from the nanostructure, creating thrust.

Numerical simulations and experimental results show that asymmetric nanostructures can resonate strongly within the visible spectrum. The resonance peak of the experimental optical characterization agrees well with our computed model, showing an 11.2% difference. However, the off resonance behavior exhibits peak broadening where the variation of intensity with wavelength, off resonance, has an experimental slope that is 3.7 times less steep than the computed model. Furthermore, the optical transmittance of the sample is 2.1 times higher than computationally modeled. Better agreement between the computed model and the experiment can be achieved by further reducing the fabrication error of the nanostructures. As seen in the experimental characterization, resonance with the incident light is polarization dependent; therefore, if the potential profile is resonance dependent, it could be possible for the potential profile to be tuned by changing the polarization of the incident light, thereby changing the trapping location of nearby nanoparticles. Polarization dependent dynamics of

nanoparticles trapped by surface plasmon resonant interactions has been observed already in Tsai's work [66].

By way of the manufacturing process, we found that certain operating parameters increased the quality of our fabricated nanostructures. We determined that charge accumulation on the sample was inevitable due to the glass substrate and that low beam currents such as 10 μA, when using the backscatter detector, or 1.4 nA, when using the secondary electron detector, helped in reducing the observed charge accumulation. We concluded that use of the backscatter electron detector produced images with half the observed manufacturing error (avg. 26.2 %) than images produced with the secondary electron detector (avg. 55.9 %). We also concluded that the quality of the nanostructures is highly dependent upon the resolution of the FIB, which is a qualitative parameter.

Using ITO or AZO to construct the nanostructures provides high thermal stability which will be of use in high optical intensity environments. They also produce a strong localized electric field with a range of only 8 MV/m over the wavelength domain of 450 nm to 1000 nm whereas Au and GaAs have more than twice the range at 18 MV/m. This increased stability in the electric field magnitude of ITO and AZO make them attractive for broad-band applications. The Au nanostructures maintain their maximum average electric field of approximately 27.5 MV/m in the y-direction for the greatest domain of incident wavelengths (650 – 1000 nm) in spite of a more varied response with the bulk electron resonance occurring at high frequency. Finally, even though GaAs has a higher melting point temperature than Au, without convective heat transfer, it conducts energy poorly compared to the other materials and is therefore least suited for high intensity optical excitation in a vacuum environment.

Finally, in the dynamic excitation modeling we developed, investigated, and presented a method to achieve nanoparticle acceleration with the surface plasmon resonance setup that we were investigating by using pulsed light rather than continuous light. We also showed that the nanoparticle experiences diminishing returns from the applied acceleration of each nano-unit as its velocity increases.

From our investigations into the plasmon linac wakefield accelerator for acceleration of ions, we found that there is a minimum phase velocity (maximum wavenumber) at which the SPP's can couple to the particles due to limits in how slow the plasmon waves can be made to propagate. Ions will need to be accelerated by a mechanism other than plasmon acceleration up to a velocity of approximately $c/5$ before they can couple with the SPP's. Furthermore, we found that as the wavenumber of the interaction regime between the SPP's and the particles becomes increasingly large, the plasmon dispersion plateaus and the SPP's become surface plasmons with zero group velocity. Implying, that if a mechanism can be contrived to slow the SPP's further and allow them to interact with particles travel less then $c/5$, they will become unable to transfer energy to the particles. In summary, these results mean that a different accelerating mechanism should be studied for use in accelerating non-relativistic particles. Such schemes may include the use of a photonic metamaterial to confine and slow the light waves rather than using a plasmonic structure.

Lastly, we have investigated a dielectrophoretic nanoparticle injection mechanism that can couple with a photonic acceleration/manipulation platform. The injector consists of tilted plates that are electrically isolated and charged to maintain a steady, nonuniform electric field across a vacuum or liquid-filled gap. We have analytically and numerically

modeled the electric field and dielectrophoretic force within the space between the tilted plates. Our results indicate that an injector with small plate angle, $\theta = 3.5°$, and narrow plate separation distance, $g = 7.0\ \mu m$, will produce stronger DEP force fields than an injector with large plate angle, $\theta \cong 82°$, and wide separation distance, $g = 15\ \mu m$. This selection will provide a maximum y-force magnitude of $50\ mN/m^3$ and an average y-force of $4.6\ \mu N/m^3$. We also conclude that choosing small $\theta = 3.5°$ and $g = 7.0\ \mu m$ will increase the amount by which the fields vary and deviate from the average within the guide sleeve such that the standard deviation of the y-force is $280\ \mu N/m^3$. We conclude that the nanoparticles must be suspended in a medium with dielectric constant greater than that of the nanoparticles so that the metallic membrane acting as a floating potential and gate will aid their motion and not hinder it. Furthermore, we developed a particle dynamics model to calculate the thrust produced by the system and found that the thrust was non-uniform over the acceleration period. It produced a total amount of thrust on the order of 550 pN over a time period of 100 μs for a simulated system of 72,050 particles.

REFERENCES

1 Bradford, J. in SpaceWorks.

2 Williams, C., Doncaster, B. & Shulman, J. (SpaceWorks Enterprises, Inc., 2018).

3 DelPozzo, S., Williams, C. & Doncaster, B. (SpaceWorks Enterprises, Inc., 2019).

4 Micci, M. M. & Ketsdever, A. D. in Progress in Aeronautics and Astronautics Vol. 187 (ed Paul Zarchan) (American Institute of Aeronautics and Astronautics, Inc., Reston, VA, 2000).

5 Barns, P., Cockcroft, J. K., Jacques, S. & Vickers, M. How Do Synchrotrons Work?, <http://pd.chem.ucl.ac.uk/pdnn/inst2/work.htm> (1997).

6 Wilson, E. An Introduction to Particle Accelerators. 1-20 (Oxford University Press Inc., 2001).

7 Cowan, B. M. Two-dimensional photonic crystal accelerator structures. Physical Review Special Topics - Accelerators and Beams **6**, 101301 (2003).

8 Naranjo, B., Valloni, A., Putterman, S. & Rosenzweig, J. B. Stable charged-particle acceleration and focusing in a laser accelerator using spatial harmonics. Physical Review Letters **109**, 164803 (2012).

9 Pae, K. H., Choi, I. W. & Lee, J. Self-mode-transition from laser wakefield accelerator to plasma wakefield accelerator of laser-driven plasma-based electron acceleration. Physics of Plasmas **17**, 123104 (2010).

10 Bar-Lev, D. & Scheuer, J. Plasmonic metasurface for efficient ultrashort pulse laser-driven particle acceleration. Physical Review Special Topics - Accelerators and Beams **17**, 121302 (2014).

11 Mizrahi, A. & Schächter, L. Optical bragg accelerators. Physical Review E **70**, 016505 (2004).

12 Passoni, M., Bertagna, L. & Zani, A. Target normal sheath acceleration: theory, comparison with experiments and future perspective. New Journal of Physics **12**, 045012 (2010).

13 Roth, M. & Schollmeier, M. in Proceedings of the CAS-CERN Accelerator School: Plasma Wake Acceleration.

14 Gramotnev, D. K. & Bozhevolnyi, S. I. Plasmonics beyond the diffraction limit. Nature Photonics **4**, 83-91 (2010).

15 Juan, M. L., Righini, M. & Quidant, R. Plasmon nano-optical tweezers. Nature Photonics **5**, 349-356 (2011).

16 Shoji, T. & Tsuboi, Y. Plasmonic optical tweezers toward molecular manipulation: tailoring plasmonic nanostructure, light source, and resonant trapping. Journal of Physical Chemistry Letters **5**, 2957-2967 (2014).

17 Shalin, A. & Sukhov, S. Plasmonic nanostructures as accelerators for nanoparticles: optical nanocannon. Plasmonics **8**, 625-629 (2012).

18 Shalin, A. S. Optical accelerator of nanoparticles. Journal of Communications Technology and Electronics **56**, 976-984 (2011).

19 Maser, J. N., Rovey, J. L., Yang, X., Li, L., Deng, H. Fabrication of asymmetric nanostructures for plasmonic space propulsion. 54th Aerospace Sciences Meeting (2016).

20 Maser, J. N., Li, L., Deng, H., Yang, X. & Rovey, J. L. Transmission spectrum of asymmetric nanostructures for plasmonic space propulsion. Journal of Spacecraft and Rockets **53**, 998-1000 (2016).

21 Rovey, J. L., Friz, P. D., Hu, C., Glascock, M. S. & Yang, X. Plasmonic force space propulsion. Journal of Spacecraft and Rockets **52**, 1163-1168 (2015).

22 El-Brolossy, T. A. et al. Shape and size dependence of the surface plasmon resonance of gold nanoparticles studied by photoacoustic technique. European Physical Journal: Special Topics **153**, 361-364 (2008).

23 Mock, J. J., Barbic, M., Smith, D. R., Schultz, D. A. & Schultz, S. Shape effects in plasmon resonance of individual colloidal silver nanoparticles. Journal of Chemical Physics **116** (2002).

24 Naik, G. V. & Boltasseva, A. Semiconductors for plasmonics and metamaterials. physica status solidi rapid research letters **4**, 295-297 (2010).

25 Wang, Y., Capretti, A. & Negro, L. D. Wide tuning of the optical and structural properties of alternative plasmonic materials. Optical Materials Express **5**, 2415-2430 (2015).

26 Abb, M., Albella, P., Aizpurua, J. & Muskens, O. L. All-optical control of a single plasmonic nanoantenna -ITO hybrid. Nano Lett. **11**, 2457-2463 (2011).

27 Dao, T. D. et al. Selective thermal emitters with infrared plasmonic indium tin oxide working in the atmosphere. Optical Materials Express **9**, 2534-2544 (2019).

28 Eldlio, M., Che, F. & Cada, M. Drude-Lorentz Model of Semiconductor Optical Plasmons. (Springer Science+Business Media, Dordrecht, 2014).

29 Zeman, E. J. & Schatz, G. C. An accurate electromagnetic theory study of surface enhancement factors for silver, gold, copper, lithium, sodium, aluminum, gallium, indium, zinc, and cadmium. Journal of Physical Chemistry **91**, 634-643 (1987).

30 Etchegoin, P. G., Le Ru, E. C. & Meyer, M. An analytic model for the optical properties of gold. The Journal of Chemical Physics **125** (2006).

31 Basic Parameters of Gallium Arsenide (GaAs), <http://www.ioffe.ru/SVA/NSM/Semicond/GaAs/basic.html>

32 Energy band gap Eg of GaAs, <https://www.batop.de/information/Eg_GaAs.html>

33 Raymond, A., Robert, J. L. & Bernard, C. The electron effective mass in heavily doped GaAs. Journal of Physics C: Solid State Physics **12** (1979).

34 Huggard, P. G., Cluff, J. A., Moore, G. P., Shaw, C. J. & Andrews, S. R. Drude conductivity of highly doped GaAs at terahertz frequencies. Journal of Applied Physics **87** (2000).

35 Askari, H., Fallah, H., Askari, M. & Mohmmadieyh, M. C. Electrical and optical properties of ITO thin films prepared by DC magnetron sputtering for low-emitting coatings. (2014).

36 D'Elia, S. et al. Ellipsometry investigation of the effects of annealing temperature on the optical properties of indium tin oxide thin films studied by Drude-Lorentz model. Applied Surface Science **255**, 7203-7211 (2009).

37 Galca, A. C., Secu, M., Vlad, A. & Pedarnig, J. D. Optical properties of zinc oxide thin films doped with aluminun and lithium. Thin Solid Films **518**, 4603-4606 (2010).

38 Lai, W.-E., Zhu, Y.-H., Zhang, H.-W. & Wen, Q.-Y. A novel reflector of AZO thin films applicable for terahertz devices. Optical Materials **35**, 1218-1221 (2013).

39 Hsu, J.-C. & Chen, Y.-Y. Comparison of the optical and electrical properties of Al-doped ZnO films using a Lorentz model. Coatings **9** (2019).

40 Zhang, M. et al. Size-dependent melting point depression of nanostructures: nanocalorimetric measurements. Physical Review B **62**, 10548-10557 (2000).

41 Pukhov, A. & Meyer-ter-Vehn, J. Applied Physics B **74**, 355-361 (2002).

42 Saito, N. & Ogata, A. Plasmon linac: A laser wake-field accelerator based on a solid-state plasma. Physics of Plasmas **10** (2003).

43 Maier, S. A. Plasmonics: Fundamentals and Applications. 28, 42-47 (Springer Science, 2007).

44 Jackson, J. D. Classical Electrodynamics. 3rd edn, 112 (John Wiley & Sons, Inc., 1999).

45 Bozhevolnyi, S. Plasmonic Nanoguides and Circuits. 47 (Pan Stanford Publishing, 2009).

46 Griffiths, D. J. Introduction to Electrodynamics. 4th edn, 402 (Pearson Education, Inc., 2013).

47 Tsymbal, E. Y. Section 13: Optical properties of solids.

48 Sandstorm, R. Argon flouride excimer laser source for sub-0.25 mm optical lithography. Optical/Laser Microlithography IV **1463**, 610-616 (1991).

49 Mixing after doubling. Sirah Lasertechnik: Agentur Fur Kommunikation & Design (2016).

50 Nave, R. Grating intensity comparison. Diffraction Grating Intensities (2016).

51 Hibbins, A. P. Grating coupling of surface plasmon polaritons at visible and microwaave frequencies. (1999).

52 Pedrotti, F. L., Pedrotti, L. S. & Pedrotti, L. M. Introduction to Optics. 3rd edn, 128 (Pearson Prentice Hall, 2007).

53 Kaler, K. V. I. S., Prakash, R. & Chugh, D. Liquid dielectrophoresis and surface microfuidics. Biomicrofluidics **4** (2010).

54 Park, S.-Y., Kalim, S., Callahan, C., Teitell, M. & Chiou, E. A light-induced dielectrophoretic droplet manipulation platform. Lab on a chip **9**, 3228-3235 (2009).

55 Fan, S. K., Chen, W. J., Lin, T. H., Wang, T. T. & Lin, Y. C. Reconfigurable liquid pumping in electric-field-defined virtual microchannels by dielectrophoresis. Lab on a chip **9**, 1590-1595, doi:10.1039/b900790c (2009).

56 Wang, K.-L., Jones, T. B. & Raisanen, A. Dynamic control of DEP actuation and droplet dispensing. J. Micromech. Microeng. **17**, 76-80 (2007).

57 Gunji, M., Jones, T. B. & Washizu, M. Dielectrophoretic microfluidic devices.

58 Pethig, R. Review article—dielectrophoresis: status of the theory, technology, and applications. Biomicrofluidics **4**, 022811, doi:10.1063/1.3456626 (2010).

59 Duff, J. D. Dielectrophoretic precipitation of airborne particles M. Eng. thesis, University of Louisville, (2013).

60 Sagar, A. & Rose, R. in 26th Aerospace Sciences Meeting Aerospace Sciences Meetings (American Institute of Aeronautics and Astronautics, 1988).

61 Constantinides, G. et al. Quantifying deformation and energy dissipation of polymeric surfaces under localized impact. Materials Science and Engineering A **489**, 403-412 (2008).

62 Whitaker, S. M., Sacco, C. & Bons, J. P. in AIAA SciTech Forum (AIAA, National Harbor, MD, 2014).

63 Wen, P., Zheng, N., Nian, J., Li, L. & Shi, Q. Flux of granular particles through a shaken sieve plate. Scientific Reports **5** (2015).

64 Chen, K. et al. Flux through a hole from a shaken granular medium. Physical Review E **74** (2006).

65 Zuriguel, I., Garcimartin, A., Maza, D., Pugnaloni, L. & Pastor, J. Jamming during the discharge of granular matter from a silo. Physical Review E **71** (2005).

66 Tsai, W., Huang, J.-S. & Huang, C. Selective trapping or rotation of isotropic dielectric microparticles by optical near field in a plasmonic archimedes spiral. Nano Letters **14**, 547-552 (2014).

VITA

Jaykob Neil Maser holds an Associate's of Science degree in Science from Northwest Missouri State University, received May 2012, and a Bachelor's of Science degree in Physics with Honors from Missouri University of Science and Technology, received December 2014. This dissertation completed the requirements for him to receive a Doctor of Philosophy degree in Aerospace Engineering from Missouri University of Science and Technology which was conferred to him in December 2019.